



UNIVERSIDADE ESTADUAL DE CAMPINAS
SISTEMA DE BIBLIOTECAS DA UNICAMP
REPOSITÓRIO DA PRODUÇÃO CIENTÍFICA E INTELLECTUAL DA UNICAMP

Versão do arquivo anexado / Version of attached file:

Versão do Editor / Published Version

Mais informações no site da editora / Further information on publisher's website:

<https://arc.aiaa.org/doi/10.2514/1.J053713>

DOI: 10.2514/1.J053713

Direitos autorais / Publisher's copyright statement:

©2015 by American Institute of Aeronautics and Astronautics. All rights reserved.

DIRETORIA DE TRATAMENTO DA INFORMAÇÃO

Cidade Universitária Zeferino Vaz Barão Geraldo

CEP 13083-970 – Campinas SP

Fone: (19) 3521-6493

<http://www.repositorio.unicamp.br>



Sound and Sources of Sound in a Model Problem with Wake Interaction

William R. Wolf*

Universidade Estadual de Campinas, 13083-970 Campinas, São Paulo, Brazil

André V. G. Cavalieri†

Instituto Tecnológico de Aeronáutica, 12228-900 São José dos Campos, São Paulo, Brazil

Bruno Backes‡

Universidade Estadual de Campinas, 13083-970 Campinas, São Paulo, Brazil

Edemar Morsch-Filho§

Universidade Federal de Santa Catarina, 89218-000 Joinville, Santa Catarina, Brazil

and

João L. F. Azevedo¶

Instituto de Aeronáutica e Espaço, 12228-904 São José dos Campos, São Paulo, Brazil

DOI: 10.2514/1.J053713

Aeroacoustic predictions of a model airframe noise problem are conducted to assess the effects of wake interaction on flow and acoustic fields. Simulations of unsteady low Reynolds number flows, including both noise generation and its subsequent propagation to the far field, are performed for a configuration composed of a cylinder placed above a NACA 0012 airfoil. An assessment of cylinder position and freestream Mach number effects on sound radiation is presented. It is observed that intense interference among cylinder and airfoil dipoles occurs for all configurations analyzed. In this case, each body scatters the sound emitted by the other. For moderate Mach number flows with wake interaction, quadrupole sources become important to the total acoustic prediction, specially for the downward noise radiation. In order to investigate how wake interaction affects noise radiation, a comparison between the current model problem with a single cylinder case is presented. Results show that wake interaction becomes a major feature of the airfoil-cylinder flow, causing a faster downstream decay of convecting disturbances when compared to the isolated cylinder case. This issue is further studied using a linear stability calculation for the wake interaction problem, which shows that for higher Mach numbers, compressibility effects lead to the formation of a wave-packet structure in the wake with higher maximum amplitude, higher convection Mach number and a sudden spatial decay. Therefore, wake interaction and compressibility effects play a key role in the present model problem and are proposed as responsible for the increase of quadrupole noise radiation.

Nomenclature

a	=	speed of sound
c	=	airfoil chord
d	=	cylinder diameter
F_i	=	dipole source
f	=	FW-H surface
G	=	Green's function
H	=	Heaviside function
$H_0^{(2)}$	=	Hankel function of the second kind and order zero
i	=	imaginary unit
M	=	Mach number
p	=	pressure
Q	=	monopole source
Re_c	=	Reynolds number based on airfoil chord c
Re_d	=	Reynolds number based on cylinder diameter d
T_{ij}	=	quadrupole source (Lighthill stress tensor)

t	=	time
u_i	=	fluid velocity
U_i	=	FW-H surface velocity
x_i	=	observer position
y_i	=	source position
δ_{ij}	=	Kronecker delta
ρ	=	density
τ_{ij}	=	viscous stress
ω	=	angular frequency

Subscripts

0	=	mean value
∞	=	freestream quantity

Superscripts

$'$	=	perturbation value
$\hat{}$	=	Fourier transformed quantity

I. Introduction

IN PRACTICAL problems of interest, especially the prediction of low and moderate Mach number airframe noise, the large disparity in spatial and temporal scales between the hydrodynamic and acoustic fields makes it impractical to directly compute far-field noise. Hybrid methods have been widely utilized as a solution to this problem where the source field is computed separately from the acoustic field using an acoustic analogy. Typically, the analogy is derived from Lighthill's work [1], with the Ffowcs Williams-Hawkings [2] (FW-H) formulation commonly used in airframe noise problems. The analogy includes contributions from sources integrat-

Presented as Paper 2013-0245 at the 19th AIAA/CEAS Aeroacoustics Conference, Berlin, Germany, 27–29 May 2013; received 10 July 2014; revision received 30 October 2014; accepted for publication 13 November 2014; published online 24 March 2015. Copyright © 2014 by the American Institute of Aeronautics and Astronautics, Inc. All rights reserved. Copies of this paper may be made for personal or internal use, on condition that the copier pay the \$10.00 per-copy fee to the Copyright Clearance Center, Inc., 222 Rosewood Drive, Danvers, MA 01923; include the code 1533-385X/15 and \$10.00 in correspondence with the CCC.

*Assistant Professor, Department of Mechanical Engineering. Member AIAA.

†Assistant Professor, Department of Aeronautics.

‡Graduate Student. Student Member AIAA.

§Undergraduate Student.

¶Senior Research Engineer, Aerodynamics Division. Fellow AIAA.

ed along surfaces (monopoles and dipoles) as well as volumetric sources along boundary layer and wake regions (quadrupoles). Due to the cost of computing the volume integrals, quadrupole terms are often neglected. In low Mach number flows, this approximation should be reasonable since the effects of quadrupoles are small relative to the effects of dipoles and monopoles. However, recent studies have shown that at moderate Mach numbers, quadrupole sources can have a non-negligible effect on far-field acoustic predictions [3,4]. Additionally, it has been demonstrated that quadrupole sources have a significant impact on far-field predictions involving airframe configurations, particularly those with wake interactions [5,6].

With growing interest in noise predictions of complex airframe configurations, the issue of quadrupole noise is of paramount importance. At flight Reynolds numbers, turbulent wakes form and interact downstream of the geometries studied. In these cases, it is unclear when quadrupoles may play an important role and when they may be neglected. Casper et al. [7] show that the inclusion of quadrupole terms is necessary for accurate two-dimensional far-field predictions of a multi-element airfoil at $M_\infty = 0.2$. For this case, the large effects of quadrupole sources could be exaggerated due to the two-dimensionality of the flow. Wolf et al. [3] present results for a NACA 0012 airfoil at $M_\infty = 0.4$ showing that quadrupole effects become non-negligible at medium and high Helmholtz numbers. The previous authors also demonstrate [4] that quadrupole sources can add up to ≈ 4 dB in overall sound pressure level at upstream observer angles for moderate Mach number flows. Greschner et al. [8] studied the problem of a rod positioned upstream of an airfoil and found that quadrupole sources were dominant for high-frequency acoustic predictions. Recently, a discussion regarding the contribution of quadrupole sources in the presence of dipole sources, in terms of the acoustic intensity, was presented by Spalart [9]. It was shown that, for such case, the Mach number scaling for the quadrupole contribution is of order M_∞^2 instead of the supposed M_∞^8 .

In the present work, aeroacoustic predictions of a two-dimensional model airframe noise problem are conducted in order to assess the effects of wake interaction on both the near flow field and acoustic field. In particular, the work addresses sound generation and propagation by dipole and quadrupole sources under the influence of wake interactions. An analysis of the individual terms appearing in the Lighthill stress tensor, including estimates of the individual noise contributions from each of the separate terms, is presented. This study is performed for different flow configurations including variations in freestream Mach number, vortex shedding frequency and relative body positions. Jacob et al. [10] investigated the noise generated by a rod upstream of an airfoil using numerical simulations and presented a comparison between two-dimensional (2-D) and three-dimensional (3-D) results in terms of flow field and acoustics. As expected, they found different flow patterns and far-field noise predictions for 2-D and 3-D calculations. However, it was shown that improved acoustic predictions could be obtained for the vortex shedding frequency using a 2-D unsteady Reynolds averaged Navier–Stokes calculation and a statistical model for spanwise pressure coherence. In the present work, although simulations are performed using a two-dimensional formulation, several aerodynamic and aeroacoustic physical mechanisms are also found in three-dimensional computations of similar configurations [11]. Recently, Yu and Lele [12,13] performed direct noise calculations using large eddy simulation of a cylinder in the proximity of a NACA 0012 airfoil for a turbulent flow at $Re_c = 50,000$. Tonal noise from cylinder vortex shedding (VS) was observed leading to strong far-field quadrupole noise, similarly to results presented in this work. It is important to mention that the effects of quadrupole sources were not analyzed with respect to broadband noise [12,13].

In the current investigation, direct numerical simulations (DNS) of unsteady flows including both noise generation, and its subsequent propagation to the far field, are performed for a two-dimensional configuration composed of a cylinder placed above a NACA 0012 airfoil at 5 deg angle of incidence. Along the text, results of acoustic predictions obtained by DNS will be described as direct noise calculations (DNCs). The Reynolds number based on the airfoil

chord is set at $Re_c = 5000$ and the Reynolds number based on the diameter of the cylinder is $Re_d = 200$. Therefore, the ratio of cylinder diameter to airfoil chord is $d/c = 0.04$. An assessment of cylinder position and freestream Mach number effects on sound radiation is presented for $M_\infty = 0.1, 0.3$, and 0.5 . The investigation of the noise sources for airfoil and cylinder vortex shedding frequencies is presented using a hybrid methodology which employs DNS for near field source computations and the FW–H equation as the acoustic analogy formulation. The integrations of surface dipole and volume quadrupole source terms appearing in the FW–H formulation are accelerated by a fast multipole method [5] that incorporates convective effects. Furthermore, with the present numerical formulation, it is possible to investigate the individual contributions of the quadrupole sources and separate the surface dipole sources from the airfoil and from the cylinder. Hence, one can analyze the specific contributions of each of these terms to the total noise generation at a particular frequency. To verify the numerical solutions, acoustic prediction results obtained by DNC are compared to those computed by the FW–H equation and good agreement is observed.

The paper is organized as follows. We describe the numerical methodology for the flow simulations and acoustic predictions in Secs. II and III, respectively. An analysis of flow and acoustic fields obtained by DNS is presented in Sec. IV.B for each flow configuration. Acoustic predictions obtained by DNC and the FW–H equation are compared in Sec. IV.C. In this section, the contributions of dipole and quadrupole sources to the total noise predictions are presented for different flow configurations, and an assessment of mean flow convection effects is performed. In Sec. IV.D, the separate contributions of the terms composing the quadrupole sources are shown and Reynolds stresses are compared in terms of field plots for different frequencies. Finally, in Sec. V, we present an investigation of the noise source mechanisms in order to understand in more detail the role of compressibility and wake interaction on quadrupole sources.

II. Flow Simulations

The general curvilinear form of the compressible Navier–Stokes equations is solved in conservation form. The numerical scheme for spatial discretization is a sixth-order accurate compact scheme [14] implemented on a staggered grid. The current numerical capability allows the use of overset grids with a fourth-order accurate Hermite interpolation between grid blocks [15].

Compact finite-difference schemes are nondissipative and numerical instabilities arising from mesh nonuniformities and interpolation at grid interfaces have to be filtered to preserve stability of the numerical schemes. The high wavenumber compact filter presented by Lele [16] is applied to the computed solution at prescribed time intervals in order to control numerical instabilities. This filter is only applied in flow regions outside of boundary layers.

The time integration of the fluid equations is carried out by the fully implicit second-order scheme of Beam and Warming [17] in the near-wall region in order to overcome the time step restriction due to the usual near-wall fine-grid numerical stiffness. A third-order Runge–Kutta scheme is used for time advancement of the equations in flow regions far away from solid boundaries. No-slip adiabatic wall boundary conditions are applied along the solid surfaces and characteristic plus sponge boundary conditions are applied in the far-field locations. The numerical tool has been previously validated for several simulations of compressible flows involving sound generation and propagation [3,5,6].

Calculations are done using nondimensional quantities, using the freestream density, temperature and speed of sound as reference quantities, and the airfoil chord as reference length. Unless otherwise specified, all the results in this paper are presented using this choice of nondimensional variables.

III. Acoustic Predictions

The Ffowcs Williams–Hawkings [2] acoustic analogy formulation is used to predict the acoustic field radiated by the unsteady flow

simulations. The frequency domain FW–H equation in integral form is written, as suggested by Lockard [18], as

$$[\hat{p}'H(f)] = - \int_{f=0} \left[i\omega \hat{Q}(y)G(\mathbf{x}, \mathbf{y}) + \hat{F}_i(y) \frac{\partial G(\mathbf{x}, \mathbf{y})}{\partial y_i} \right] dS - \int_{f>0} \hat{T}_{ij}H(f) \frac{\partial^2 G(\mathbf{x}, \mathbf{y})}{\partial y_i \partial y_j} dV \quad (1)$$

where p' is the acoustic pressure, ω is the angular frequency, \mathbf{y} is a source location, \mathbf{x} is an observer location and the term $\hat{\cdot}$ represents a Fourier transformed quantity. The monopole and dipole source terms are

$$Q = [\rho(u_i + U_i) - \rho_0 U_i] \partial f / \partial x_i \quad (2)$$

and

$$F_i = [p\delta_{ij} - \tau_{ij} + \rho(u_i - U_i)(u_j + U_j) + \rho_0 U_i U_j] \partial f / \partial x_j \quad (3)$$

respectively, and T_{ij} is the Lighthill stress tensor or quadrupole source term given by

$$T_{ij} = \rho u_i u_j + (p' - a^2 \rho') \delta_{ij} - \tau_{ij} \quad (4)$$

In Eqs. (2–4), u_i is the fluid velocity vector, U_i is the FW–H surface velocity, p is the pressure, ρ_0 is the freestream density, ρ' and p' stand for the density and pressure perturbations, respectively, a is the speed of sound, δ_{ij} is the Kronecker delta and τ_{ij} is the viscous stress tensor. The term $f = 0$ represents the FW–H surface and $H(f)$ is the Heaviside function defined as $H(f) = 1$ for $f > 0$ and $H(f) = 0$ for $f < 0$. Source terms, observer locations and scattering bodies are assumed to be in steady uniform motion with $\mathbf{U} = (-U_1, 0)'$. Therefore, the FW–H surface velocity and the mean convection speed in the observer region are completely equivalent. In summary, the present work assumes that the airfoil, cylinder and observers are stationary, and there is a uniform flow of speed U_i . The convective Green's function is given by

$$G(\mathbf{x}, \mathbf{y}) = \frac{i}{4\sqrt{1-M^2}} e^{iM \frac{k}{(1-M^2)}(x_1-y_1)} \times H_0^{(2)} \left(\frac{k}{(1-M^2)} \sqrt{(x_1-y_1)^2 + (1-M^2)(x_2-y_2)^2} \right) \quad (5)$$

where M is the freestream Mach number defined as $M \equiv U_1/a$, k is the acoustic wavenumber and $H_0^{(2)}$ is the Hankel function of the second kind and order zero.

In the present work, the surface integrations appearing in Eq. (1) are computed along the scattering body surfaces. Therefore, $u_i = -U_i$ for the monopole and dipole source terms, which are then given by $Q = -\rho_0 U_i \partial f / \partial y_i$ and $F_i = [p\delta_{ij} + \rho_0 U_i U_j] \partial f / \partial y_j$, respectively. Furthermore, one can observe that the monopole source terms, Q , and the second component of the dipole source terms, $\rho_0 U_i U_j$, are steady in time and do not appear in the frequency domain formulation.

The volume integrations in Eq. (1) are computed using a fast multipole method [5] that incorporates convective effects. Quadrupoles are computed along a rectangular region of the flow field with $-1c < x < 10c$ and $-2c < y < 3c$. This subset region includes wakes and boundary layers, where the magnitudes of quadrupole sources are non-negligible. Increasing the dimensions of the rectangular region did not affect the results since the intensities of the quadrupoles are negligible further away from these locations. In the present work, acoustic predictions can be performed for observer locations inside the subset region where quadrupoles are non-negligible. When these observers are too close to a specific quadrupole (for instance, less than $0.01c$), the effect of this particular source is not accounted in the noise prediction. One should keep in mind that the effect of a particular far-field quadrupole on a nearby observer will be high due to the singularity of the second derivative of the Hankel function in

Eq. (1). Computing the finite part of the hypersingular integral would avoid this issue but that would considerably increase the total computational cost of the acoustic prediction. Furthermore, for a far-field observer, the contribution of a particular nearby quadrupole should be negligible.

With the present numerical formulation, it is possible to investigate the individual contributions of the quadrupole sources and separate the surface dipole sources from the airfoil and from the cylinder. Hence, one can analyze the specific contributions of each of these terms to the total noise generation at a particular vortex shedding frequency.

IV. Results

A. General Description of the Test Cases

This section discusses results obtained by DNC and the FW–H equation for the unsteady flow past a cylinder in the proximity of a NACA 0012 airfoil. The flow configurations investigated allow a study of sound generation due to interaction of boundary layers and wakes, including vortex shedding. The flow Reynolds numbers based on the airfoil chord and cylinder diameter are $Re_c = 5000$ and $Re_d = 200$, respectively. The freestream Mach numbers considered in the flow calculations and acoustic predictions are $M_\infty = 0.1, 0.3$, and 0.5 , and the angle of incidence is fixed at $AoA = 5^\circ$.

The present grid configuration consists of body-fitted O -grid blocks around airfoil and cylinder surfaces and a background O -grid block that resolves the acoustic far field. The airfoil grid block is composed of 400×60 grid points, in the periodic and wall normal directions, respectively, and the cylinder grid block is composed of 240×50 grid points, in the periodic and wall normal directions. These grid blocks are designed to accurately resolve the laminar boundary layers that develop along the airfoil and cylinder surfaces. The far-field background grid block has 400×625 points, in the periodic and wall normal directions, respectively, with smooth stretching to accurately capture the sound radiation. It should be observed that the previously described mesh was the result of a grid convergence study in terms of both flow and acoustic fields. In this study, far-field sound was predicted for different mesh configurations and the selected grid has yielded adequate resolution for sound prediction in all frequencies of interest in the present study. The background grid block has approximately $15c$ of distance from the airfoil mid-chord. A sponge region is applied along the last $3.5c$ of the mesh in order to damp out reflections of acoustic waves.

To evaluate the effects of cylinder position on acoustic reflection and diffraction, the cylinder grid block is displaced from the half-chord position to the trailing-edge position. A summary of the flow configurations investigated is presented in Table 1. In Figs. 1a and 1b, one can see the geometries analyzed with the cylinder at half-chord and trailing-edge positions, respectively. Several parameters used in the computation of statistics for the configurations analyzed are provided in Table 2. In this table, Δt is the nondimensional time step used in the simulations, F_s is the nondimensional sampling frequency for the Fourier analysis, NS is the number of samples used in the Fourier analysis, and TR is the total time record used for statistics.

In the present study, the NACA 0012 airfoil has normalized chord $c = 1$ with trailing edge at $(x, y) = (1.0c, 0.0)$. Since the airfoil is at

Table 1 Summary of flow configurations investigated

Configuration	Mach number	Cylinder center $(x, y)^b$	St_d^a	St_c^a
1	$M_\infty = 0.1$	$(0.5c, 0.25c)$	0.21	—
2	$M_\infty = 0.3$	$(0.5c, 0.25c)$	0.21	—
3	$M_\infty = 0.5$	$(0.5c, 0.25c)$	0.20	—
4	$M_\infty = 0.1$	$(1.0c, 0.25c)$	0.20	1.80
5	$M_\infty = 0.3$	$(1.0c, 0.25c)$	0.20	1.80
6	$M_\infty = 0.5$	$(1.0c, 0.25c)$	0.20	1.80
7	$M_\infty = 0.3$	$(0.0c, 0.0c)$	0.20	—
8	$M_\infty = 0.5$	$(0.0c, 0.0c)$	0.20	—

^aThe cylinder and airfoil Strouhal numbers are $St_d = fd/U_\infty$ and $St_c = fc/U_\infty$, respectively.

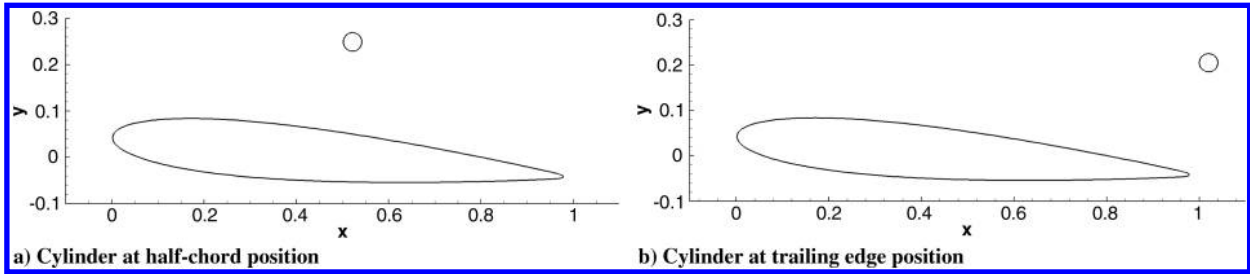


Fig. 1 Detail view of the configurations analyzed.

$\text{AoA} = 5^\circ$, figures show the configuration rotated by -5° . All directivity plots are presented for a coordinate system located at the airfoil half-chord position. In order to further investigate the changes in cylinder wake structure, simulations of the flow past an isolated cylinder are also performed. In this case, the flow Reynolds number based on the cylinder diameter is $Re_d = 200$ and the freestream Mach numbers considered are $M_\infty = 0.3$ and 0.5 . The grid configuration consists of a body-fitted O -grid block around the cylinder composed of 400×1000 grid points, in the periodic and wall normal directions. Results of acoustic predictions are presented for observer locations at $r/c = 5$ for the low Mach number flows (or low frequencies). These positions are at least two acoustic wavelengths distant from the source region. For the higher Mach number cases, the acoustic wavelengths are shorter and, therefore, acoustic predictions are presented at closer observer positions at $r/c = 2$ to guarantee the accuracy of the DNCs. For these cases, observers are in a “quasi far field,” between three and six acoustic wavelengths away from the source region for $M_\infty = 0.3$ and 0.5 , respectively. For case 6 at $M_\infty = 0.5$, acoustic predictions are also shown for far-field observers at $r/c = 100$.

B. Flow and Acoustic Fields

Figures 2–4 present snapshots of the flow and acoustic fields obtained by DNS for all configurations analyzed. Contours of z -component of vorticity along the airfoil and cylinder wake regions are shown together with contours of dilatation. These figures allow a preliminary analysis of the effects of cylinder position and freestream Mach number on sound generation and propagation. In Figs. 2a and 2b, one can observe the presence of vortex shedding forming along the cylinder and airfoil wakes for both cylinder positions investigated for $M_\infty = 0.1$. For flow configurations with freestream Mach numbers $M_\infty = 0.3$ and 0.5 , Figs. 3 and 4, respectively, different hydrodynamic features are observed due to a change in cylinder position. When the cylinder is placed at half-chord, the airfoil vortex shedding is suppressed due to wake interaction. For this cylinder position, it is also observed that cylinder vortex shedding ceases further upstream as Mach number is increased. If the cylinder is placed at the trailing-edge position, airfoil vortex shedding is developed for the entire range of Mach numbers analyzed. For all tested cases, one can notice that further downstream along the wake, there is a merging of alternating vortical structures which characterizes a single vortex shedding frequency.

Table 2 Parameters used in the computation of statistics for the configurations analyzed

Configuration	Δt	F_s	NS	TR
1	0.0004	25	1024	40.96
2	0.0004	50	512	10.24
3	0.0002	50	512	10.24
4	0.0004	25	1024	40.96
5	0.0004	50	512	10.24
6	0.0002	50	512	10.24
7	0.0005	8	512	64.0
8	0.00025	8	512	64.0

Far-field sound radiation is also modified according to freestream Mach number and cylinder position. From Figs. 2–4, it is clear that Mach number effects considerably modify the acoustic wave-numbers. Higher Mach numbers are associated to higher frequencies with lower acoustic wavelengths. Doppler effects are also readily seen, specially in Fig. 4, for $M_\infty = 0.5$. The cylinder position impacts the scattering characteristics of the acoustic field. In Figs. 2a, 3a, and 4a, it is possible to see the more pronounced reflection effects along the airfoil surface by the formation of a shadow zone below the airfoil and, in Figs. 2b, 3b, and 4b, one can observe that trailing-edge diffraction effects are more prominent. Figure 5 shows spectra of acoustic perturbations obtained for an observer positioned at $(x, y) = (0.5c, 1.0c)$. The measured signals are periodic although the vorticity and acoustic fields exhibit complex patterns in Figs. 2 and 4. Results obtained for freestream Mach numbers $M_\infty = 0.1$ and 0.5 are shown in Figs. 5a and 5b, respectively. In the next section, noise predictions will be presented for Helmholtz numbers $kc = 3.4$ and $kc = 3.2$ shown in Fig. 5a, and for $kc = 16.0$ and $kc = 15.3$, shown in Fig. 5b. These values of kc correspond to the cylinder vortex shedding frequencies of cases 1 and 4, and 3 and 6, respectively. The tonal peaks associated with these frequencies are the higher peaks appearing in the spectra of Figs. 5a and 5b.

In Figs. 6–8, one can see plots of mean velocity magnitude normalized by freestream velocity for $M_\infty = 0.1, 0.3$, and 0.5 , respectively. In these figures, streamlines along airfoil and cylinder wakes are also shown in order to visualize the flow variations due to freestream Mach number and cylinder position. One can see in Figs. 6 and 7 that, when the cylinder is moved to the airfoil trailing edge, flow reversal starts upstream and the separation bubble which forms along the airfoil suction side becomes larger. One can see in Fig. 8 that the flow does not separate for $M_\infty = 0.5$ when the cylinder is at half-chord position.

Increasing the freestream Mach number implies large modifications in the flow along the cylinder wake as can be observed in Figs. 7a and 8a, specially when the cylinder is located at $x/c = 0.5$. For all cases analyzed, the cylinder “near wake” is similar to that of a single cylinder in a viscous laminar flow. However, further downstream, after momentum starts recovering, the wake exhibits another region of momentum loss. This effect becomes more pronounced as the freestream Mach number gets higher. Although this effect can be observed for both cylinder positions, it is more noticeable when the cylinder is placed above the airfoil half-chord. Furthermore, it is stronger for $M_\infty = 0.5$ and one can even notice the presence of a flow separation region along the cylinder wake. This effect is called “off-body separation” and it appears when a wake develops under an adverse pressure gradient [19,20]. Here, the adverse pressure gradient is due to the flow along the suction side of the airfoil. In Fig. 8a one can see that the boundary layer is fully attached along the airfoil suction side due to the flow acceleration under the cylinder wake. Even for the low and moderate Mach numbers analyzed, compressibility plays an important role for the present problem with wake interaction. It could be possible that the low Reynolds number impacts the off-body separation appearing Fig. 8a. It would be interesting to investigate a similar configuration at a higher Reynolds number, with the development of a turbulent boundary layer. Recently, simulations of similar flow configurations were performed for turbulent flows at $Re_c = 50,000$ [12,13]. In these references, however, no analysis was provided in terms of the mean flow field.

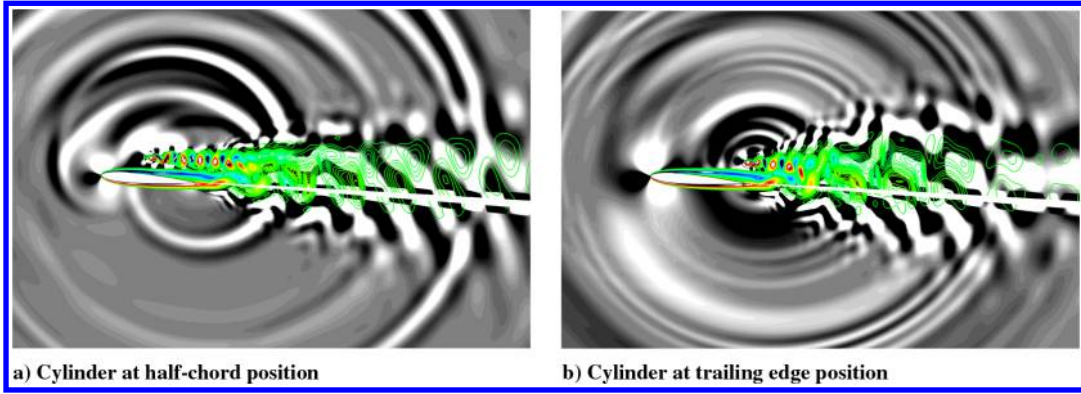


Fig. 2 Contours of z -vorticity and contours of dilatation for $M_\infty = 0.1$.

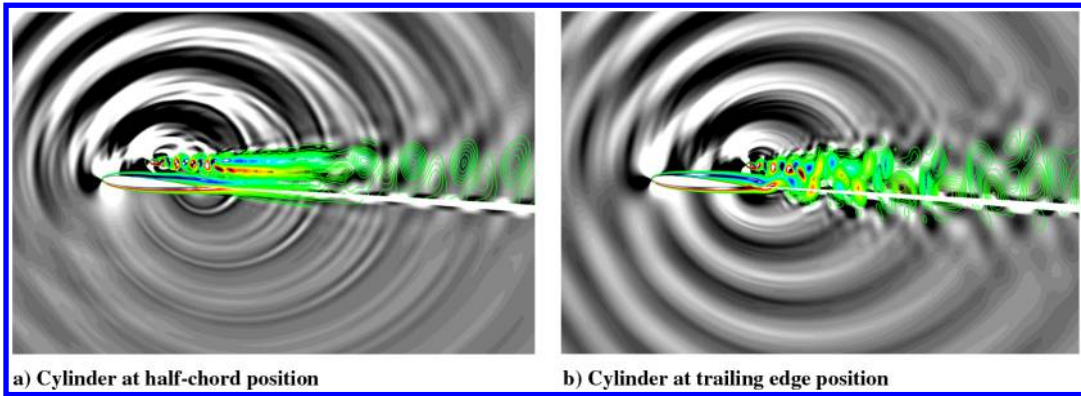


Fig. 3 Contours of z -vorticity and contours of dilatation for $M_\infty = 0.3$.

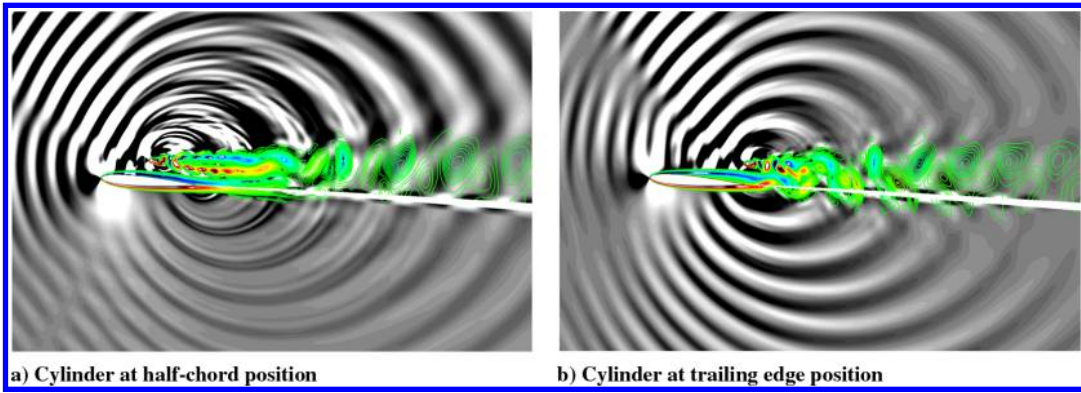


Fig. 4 Contours of z -vorticity and contours of dilatation for $M_\infty = 0.5$.

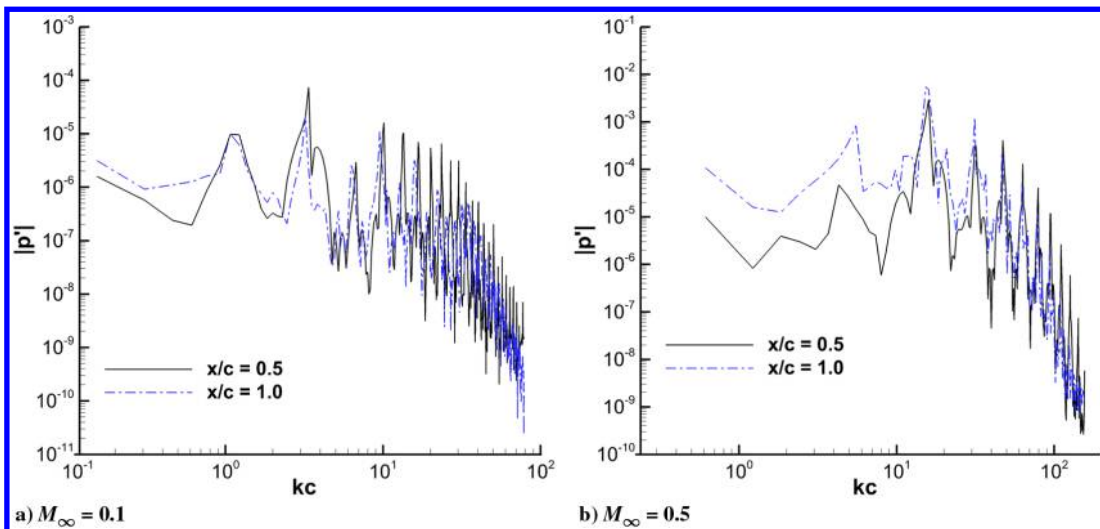


Fig. 5 Spectra of pressure perturbation obtained for an observer positioned at $(x,y) = (0.5c,1.0c)$.

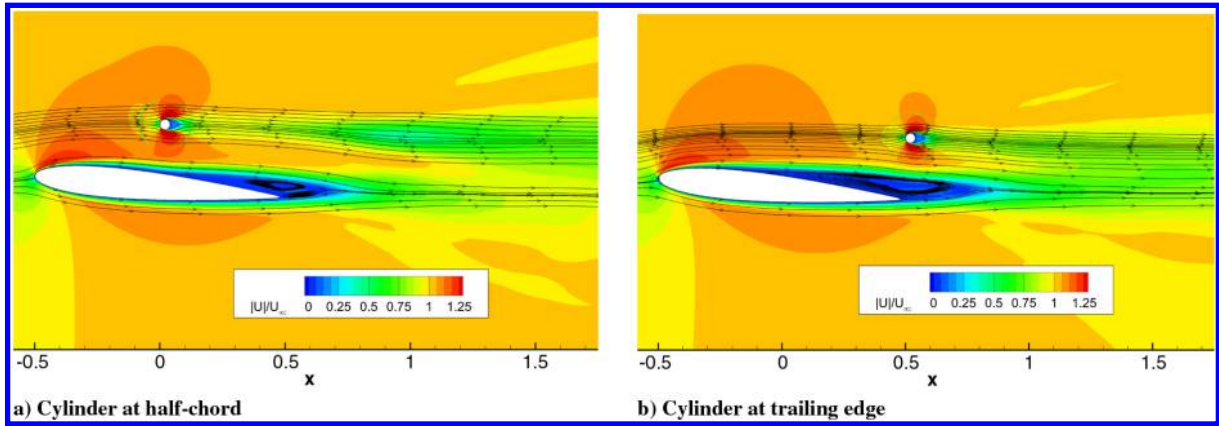


Fig. 6 Mean velocity magnitude normalized by freestream velocity and streamlines for $M_\infty = 0.1$.

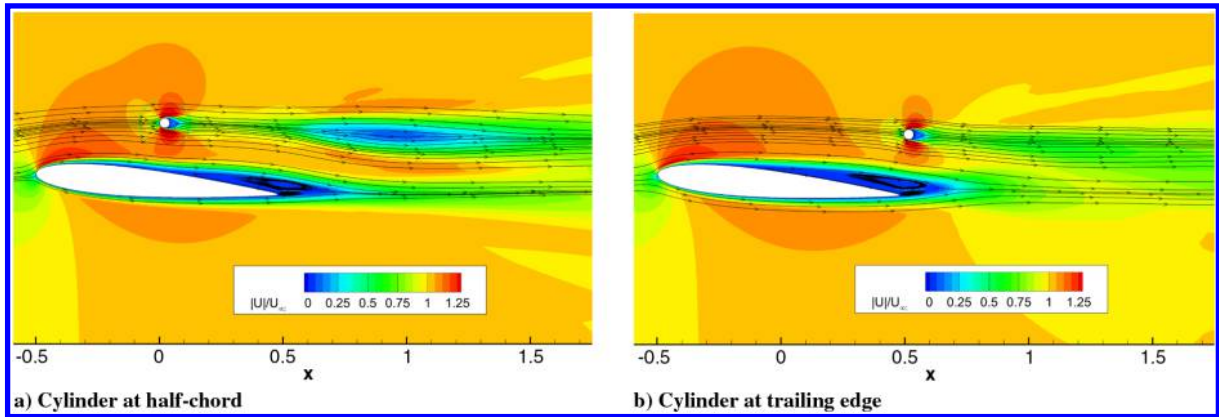


Fig. 7 Mean velocity magnitude normalized by freestream velocity and streamlines for $M_\infty = 0.3$.

C. Noise Predictions

Figure 9 presents the acoustic predictions for the cylinder vortex shedding frequency for case 1. Here, the cylinder is located above the airfoil half-chord and the freestream Mach number is $M_\infty = 0.1$. In Fig. 9a, one can see the Fourier transformed acoustic field obtained by DNC. At the cylinder vortex shedding frequency, the chord based Helmholtz number is given by $He = kc = 3.4$ and the cylinder Strouhal number is $St_d = fd/U_\infty = 0.21$. Along the text, the Helmholtz numbers are calculated based on the airfoil chord in order to provide information of airfoil acoustic compactness. One should see that the cylinder can be considered as a compact source since its diameter is considerably smaller than the acoustic wavelengths for all frequencies investigated.

For the cylinder VS frequency, the acoustic field is composed by acoustic waves that are generated by the cylinder and are either

reflected upwards by the airfoil surface or diffracted along the airfoil trailing edge. In Fig. 9b, one can observe a directivity plot of acoustic pressures obtained for the separate noise sources including the airfoil and cylinder dipoles and the volume quadrupoles. In the plot, observer positions are at $r = 5c$. As expected for such a low Mach number problem, acoustic radiation is dominated by dipole sources and quadrupole sources can be neglected in the far-field acoustic prediction. Figure 9b also shows that, for the present low frequency problem, the dipolar acoustic fields from airfoil and cylinder are similar to those expected from a free-field Green's function [21]. In the same figure, one can also see that both dipole sources present similar amplitudes in terms of sound radiation. Despite the fact that pressure amplitudes are similar for airfoil and cylinder dipoles, there is a phase opposition leading to a strong noise cancellation below the airfoil. This effect can be observed in Fig. 9c, when the total noise

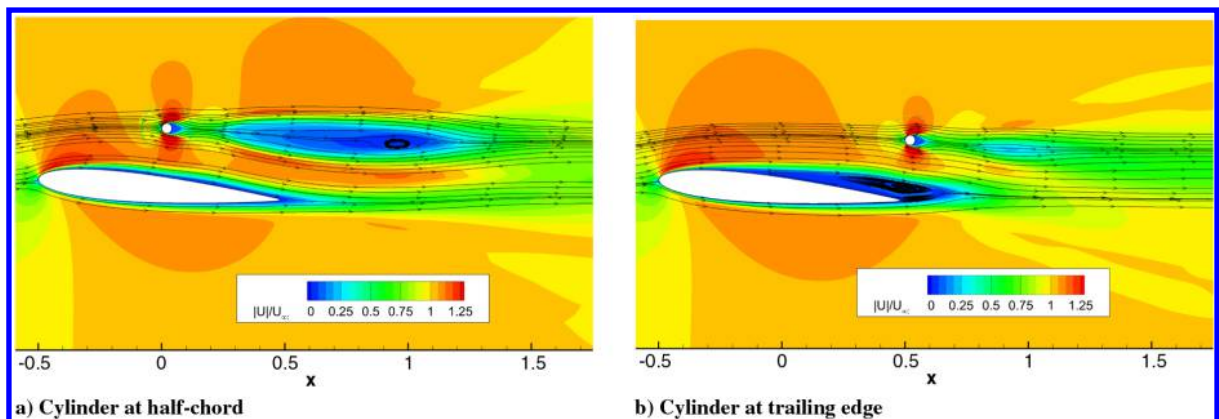


Fig. 8 Mean velocity magnitude normalized by freestream velocity and streamlines for $M_\infty = 0.5$.

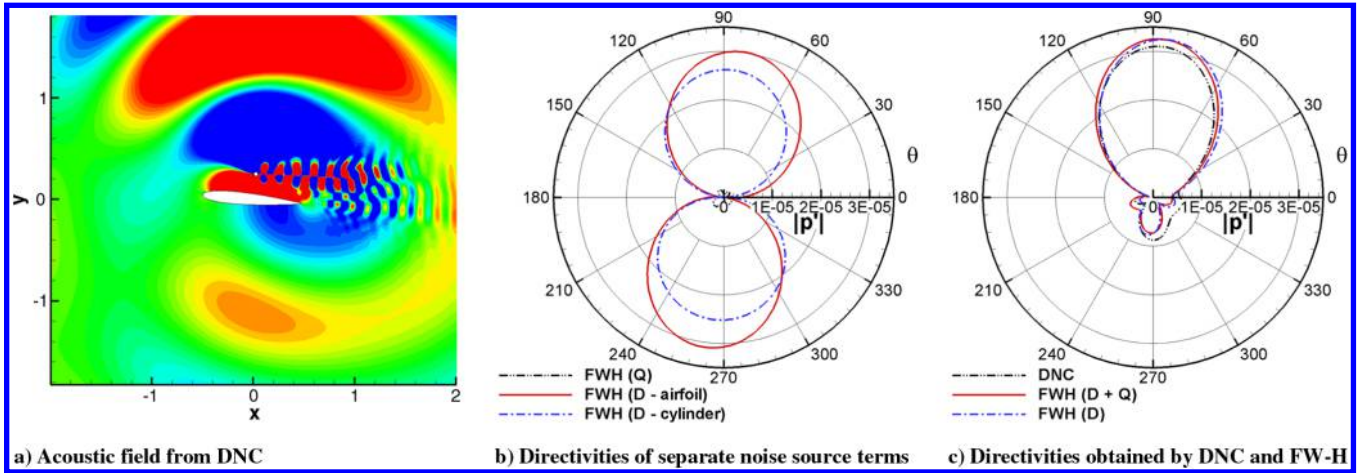


Fig. 9 Acoustic predictions for $M_\infty = 0.1$, cylinder at half-chord position and results at the cylinder vortex shedding frequency.

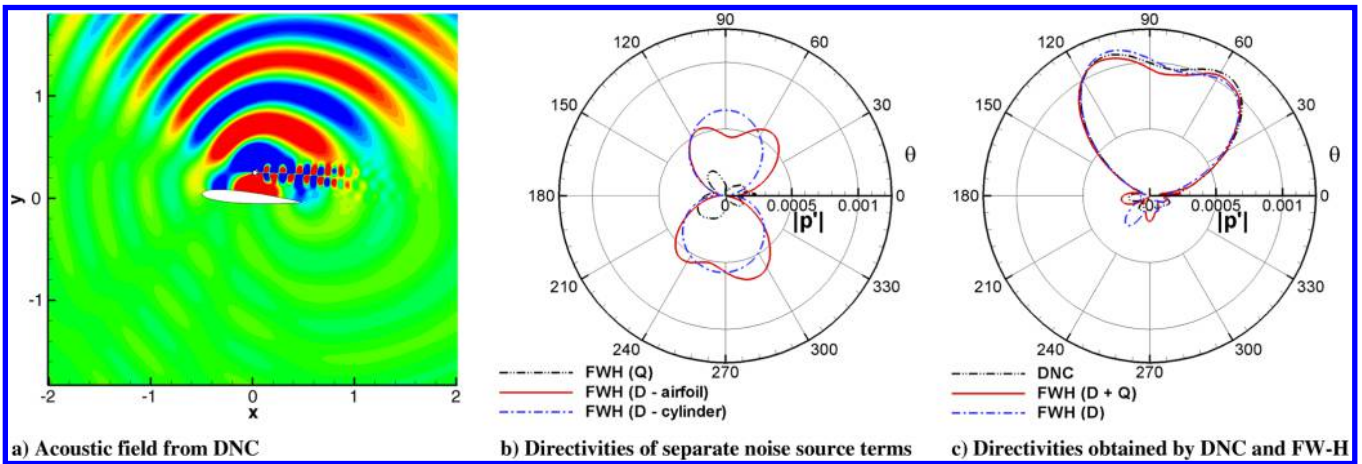


Fig. 10 Acoustic predictions for $M_\infty = 0.3$, cylinder at half-chord position and results at the cylinder vortex shedding frequency.

radiation is computed. In the same figure, one can see the good comparison in terms of acoustic pressure levels between the DNC and the FW-H solution.

In Figs. 10 and 11, one can observe the acoustic predictions for cases 2 and 3 at $M_\infty = 0.3$ and 0.5 , respectively. Similarly to case 1, the cylinder is located above the airfoil half-chord. Figures 10a and 11a present the acoustic fields obtained by DNC for the cylinder vortex shedding frequency. For cases 2 and 3, the Helmholtz and Strouhal numbers are given by $He = 9.8$ and $St_d = 0.21$, and $He = 16.0$ and $St_d = 0.20$, respectively. Similarly to case 1, the acoustic fields for the present configurations are composed by acoustic waves

generated by the unsteady loading along the cylinder. However, scattering effects become more pronounced at higher Helmholtz numbers and, therefore, they considerably modify the acoustic fields. While acoustic waves are mainly reflected upwards for case 2, they are reflected in several directions for case 3. Diffraction effects along leading and trailing edges can also be observed in the figures for both cases.

Since, for the present configurations analyzed, the Helmholtz numbers are larger than 2π , the airfoil behaves as a noncompact body. Such effect can be observed in the acoustic directivity plots of the separate noise sources, shown in Figs. 10b and 11b. One can see in

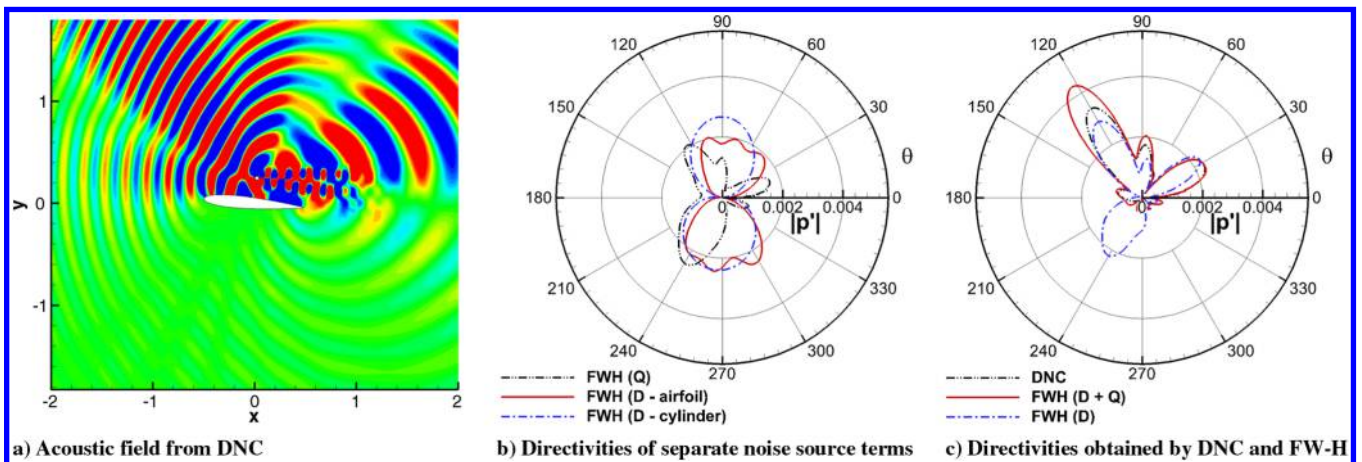


Fig. 11 Acoustic predictions for $M_\infty = 0.5$, cylinder at half-chord position and results at the cylinder vortex shedding frequency.

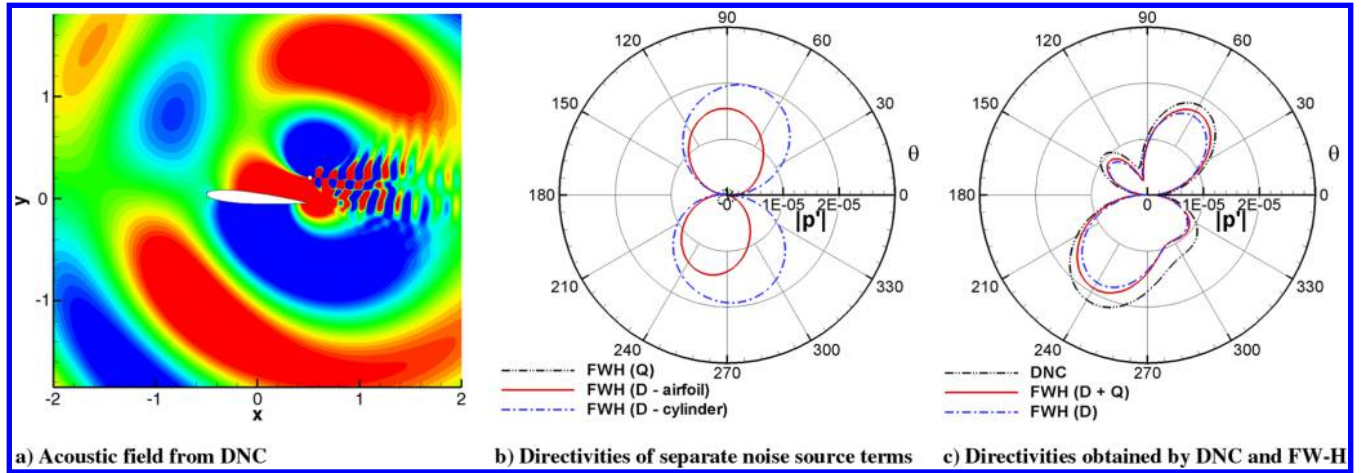


Fig. 12 Acoustic predictions for $M_\infty = 0.1$, cylinder at trailing-edge position and results at the cylinder vortex shedding frequency.

these plots that the airfoil dipole directivities, computed at $r = 2c$, resemble those from a half-plane Green's function [22]. Figures 10b and 11b present a comparison of acoustic pressure values from each separate noise source. One can see that quadrupole noise contribution becomes relevant for the present flow configurations at moderate Mach numbers. For compact sources, at low Mach numbers, one should expect the typical directivity pattern of lateral quadrupoles. This behavior is, in fact, observed in the present study for the $M_\infty = 0.1$ case in Fig. 9b. However, for higher Mach numbers, when sources become noncompact, the integration of the spatial distribution of volumetric quadrupole sources results in a directivity pattern that no longer resembles the typical compact lateral quadrupole directivity. In Figs. 10c and 11c, directivities of total acoustic pressure obtained by DNC and the FW-H are shown. The latter are computed including the effects of dipoles without quadrupoles and the combined effects of dipoles and quadrupoles. The complex radiation patterns predicted using DNC are recovered by the FW-H formulation and the full directivity pattern for $M_\infty = 0.5$ is only accurately computed if quadrupole sources are added in the FW-H equation. However, one can also observe in Fig. 11c that there are still some differences in the upstream lobes between the DNC results and those from the FW-H equation with quadrupole sources. Such differences may be due to the fact that the present acoustic analogy formulation considers a uniform flow on sound propagation. For this case, the nonuniformity of the flow could have a larger effect on sound prediction. Similar results are observed in [23] for the acoustic scattering along a multi-element airfoil.

Figures 12a–12c present the acoustic field, separate acoustic pressure directivities and total directivities computed by DNC and the FW-H equation at $r = 5c$, respectively, for case 4. Results shown in Fig. 12 are computed for the cylinder vortex shedding frequency with Helmholtz and Strouhal numbers given by $He = 3.2$ and $St_d =$

0.20, respectively. For the current flow configuration, the cylinder is positioned at the airfoil trailing edge and the freestream Mach number is $M_\infty = 0.1$. In Fig. 12a, one can observe that the acoustic field is similar to that of Fig. 9a. However, since the cylinder is displaced to the trailing-edge region, acoustic diffraction is more pronounced downwards for the present case. In Fig. 12b, one can notice that, for case 4, the amplitude of the airfoil dipole is smaller than that of the cylinder, differently from case 1. Such effect occurs since acoustic reflection along the airfoil surface is less intense. From the same figure, it is also possible to infer that quadrupole sources have negligible effect on total noise prediction for the current low Mach number. Figure 12c shows the total acoustic directivity computed by DNC and the FW-H equation. While for case 1 most of the sound field was reflected upwards by the airfoil surface, for the present case, the sound field is more intense downwards, due to the larger effect of trailing-edge diffraction.

In Figs. 13 and 14, one can observe results of acoustic predictions for case 5, for the airfoil and cylinder vortex shedding frequencies, respectively. These frequencies correspond to Helmholtz and Strouhal numbers equal to $He = 3.4$ and $St_c = 1.8$, and $He = 9.5$ and $St_d = 0.20$, respectively. Directivities for Fig. 13 are obtained at $r = 5c$ and those from Fig. 14 are computed at $r = 2c$. It is possible to see in Figs. 13a–13c that trailing-edge scattering is the noise generation mechanism for the airfoil vortex shedding frequency. For such low frequency, quadrupole sources have a small contribution to far-field radiation and the cylinder dipole can be neglected in the total noise prediction. The total acoustic directivity is typical of low frequency airfoil trailing-edge noise [3].

Similarly to the results presented for case 4, results shown in Fig. 14 for the cylinder vortex shedding frequency of case 5 demonstrate that acoustic diffraction becomes more pronounced when the cylinder is displaced towards the trailing edge. However, reflection

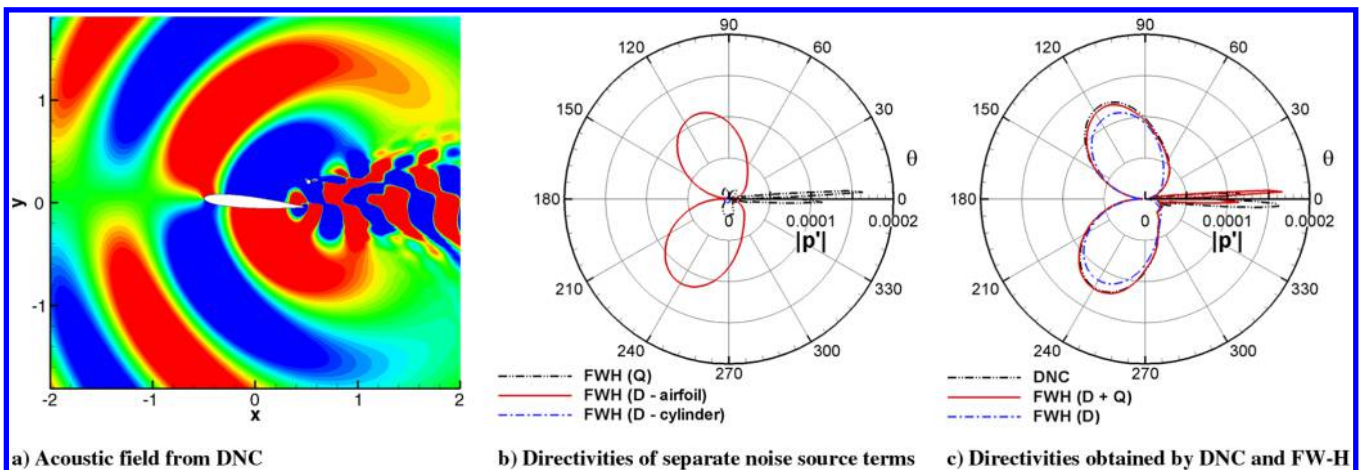


Fig. 13 Acoustic predictions for $M_\infty = 0.3$, cylinder at trailing-edge position and results at the airfoil vortex shedding frequency.

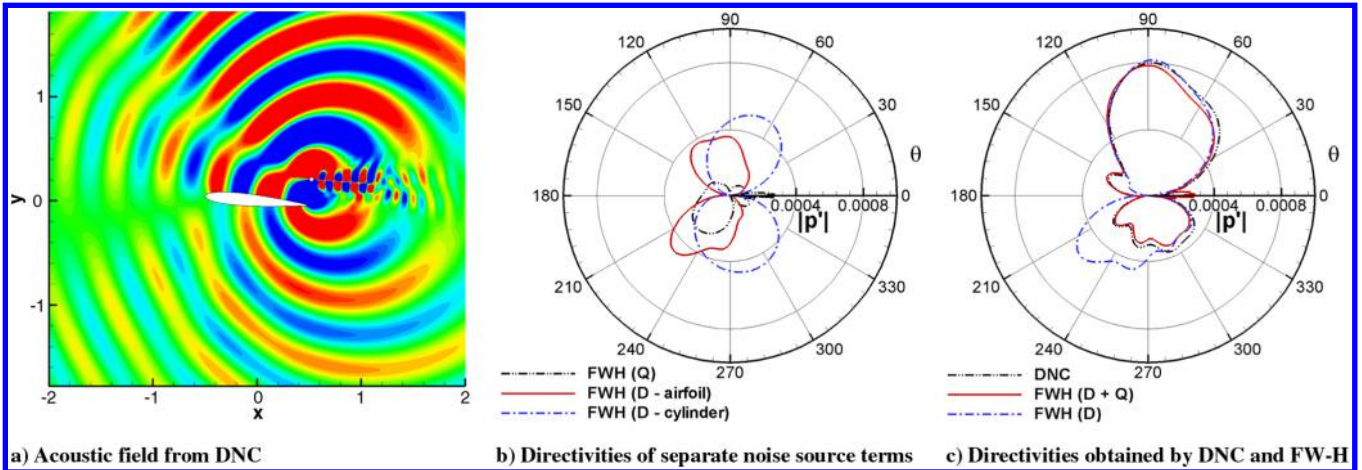


Fig. 14 Acoustic predictions for $M_\infty = 0.3$, cylinder at trailing-edge position and results at the cylinder vortex shedding frequency.

effects are still dominant in terms of total noise radiation for the current case. From visualization of Figs. 14b and 14c, one can argue that, for the present flow configuration, upward acoustic reflection occurs due to interaction of dipole sources, and diffraction effects can only be accurately predicted if quadrupole sources are included in the FW-H equation.

Figures 15 and 16 present acoustic prediction results of case 6 for the airfoil and cylinder vortex shedding frequencies, respectively. These frequencies correspond to Helmholtz and Strouhal numbers equal to $He = 5.5$ and $St_c = 1.8$, and $He = 15.3$ and $St_d = 0.20$, respectively. Directivity plots are obtained for observer positions at $r = 2c$. Similarly to Fig. 11a, in Figs. 15a and 16a, one can observe

the complex patterns of the radiated fields, composed by the incident acoustic field due to the quadrupole sources and the scattered field due to the dipole sources. Figures 15b and 15c show that, for the airfoil vortex shedding frequency, the total noise radiation is obtained by the sum of sound fields from quadrupole and airfoil dipole sources. As previously observed for case 5, the far-field noise contribution of the cylinder dipole is negligible at this frequency.

Wolf et al. [3] demonstrate that quadrupole sources are only relevant for acoustic predictions of moderate Mach number flows at high Helmholtz numbers. The present results indicate that, even at low Helmholtz numbers, quadrupole sources are of paramount importance for the total noise prediction of a moderate Mach number

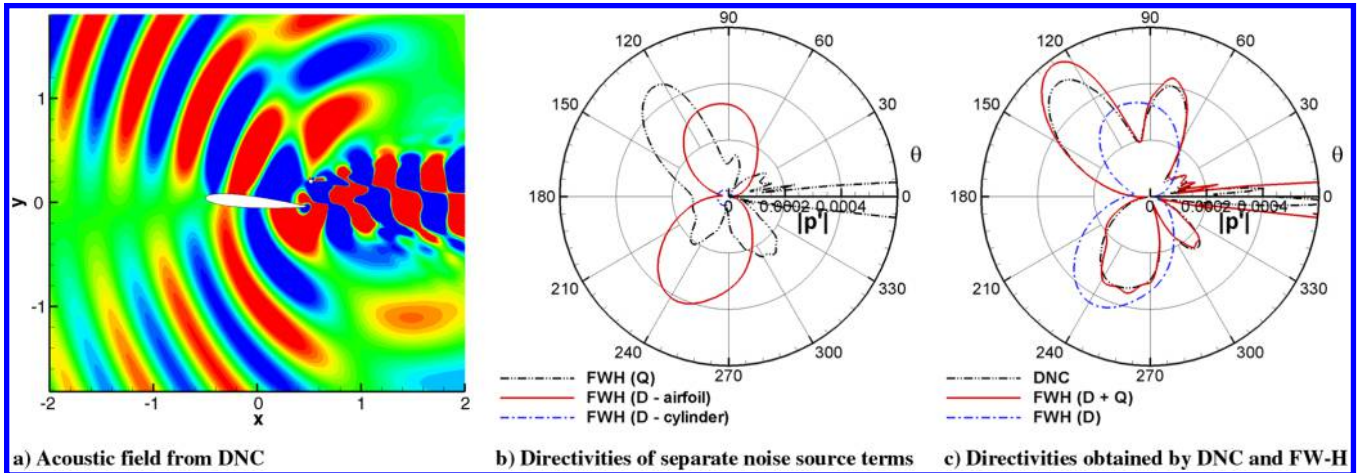


Fig. 15 Acoustic predictions for $M_\infty = 0.5$, cylinder at trailing-edge position and results at the airfoil vortex shedding frequency.

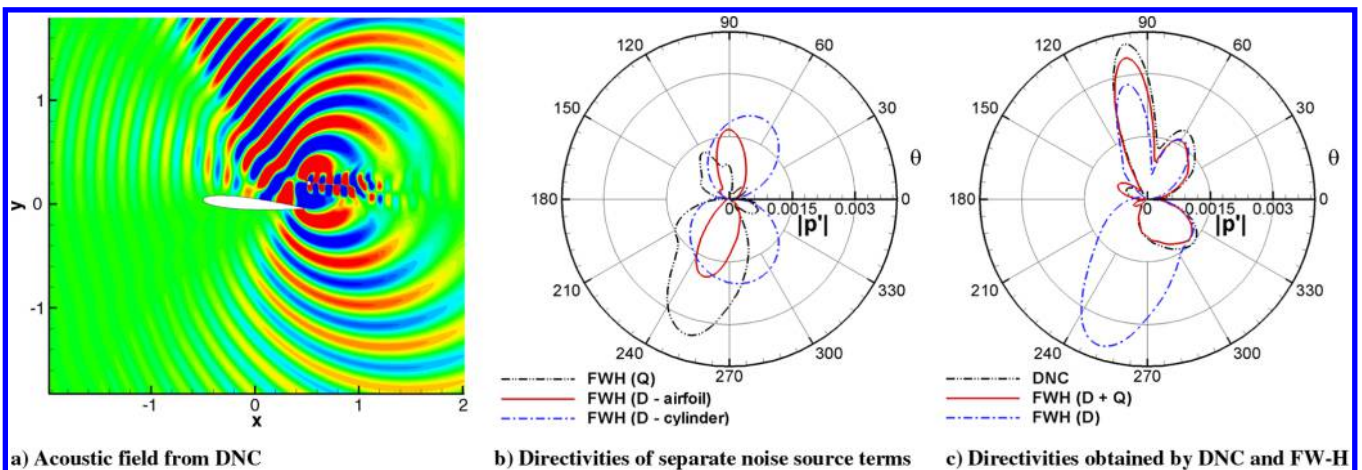


Fig. 16 Acoustic predictions for $M_\infty = 0.5$, cylinder at trailing-edge position and results at the cylinder vortex shedding frequency.

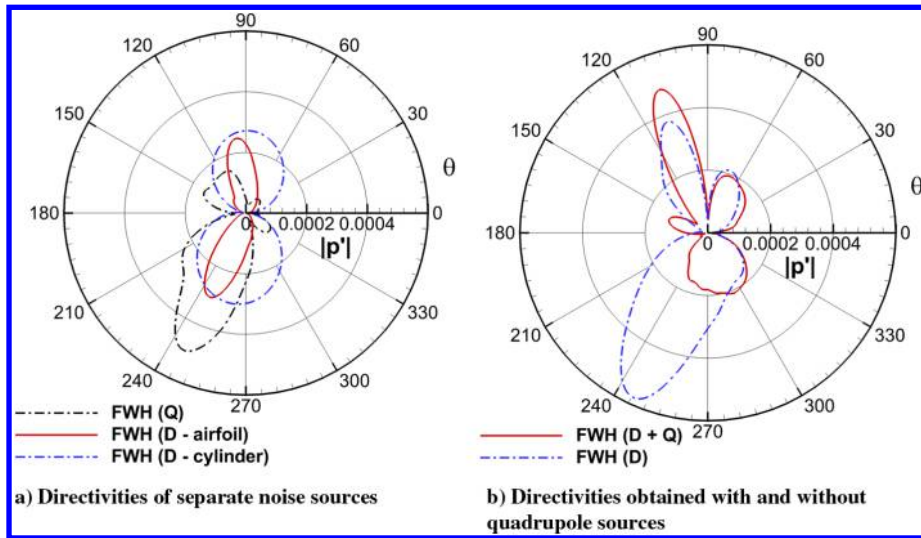


Fig. 17 Far-field acoustic predictions at $r/c = 100$ for $M_\infty = 0.5$, cylinder at trailing-edge position, at the cylinder vortex shedding frequency. Results are obtained by the FW-H acoustic analogy.

flow with wake interaction. In Figs. 15c and 16c, one can see that the noise predictions obtained by the FW-H formulation show excellent agreement with those obtained by DNC when quadrupoles are taken into account. In the latter figure, and also from Fig. 16b, for the cylinder vortex shedding frequency, one can claim that the acoustic field generated by the quadrupole sources correct the total acoustic pressure below the airfoil. Therefore, for the present Mach number, if the airfoil vortex shedding is the driving noise source mechanism, quadrupole and dipole sources are responsible for the far-field noise above and below the airfoil. However, if the cylinder vortex shedding

is the driving noise source mechanism, dipole sources are related to both acoustic reflection and diffraction. In this case, quadrupole sources are more related to a correction of the total acoustic prediction below the airfoil.

Figure 17 presents acoustic predictions for observer locations at $r/c = 100$, for case 6, at the cylinder vortex shedding frequency. With the present results, it is possible to observe the strong contributions of quadrupole sources to far-field observers. One can also see that the patterns of far-field directivities at $r/c = 100$ are similar to those from Fig. 16 and, therefore, confirm that acoustic

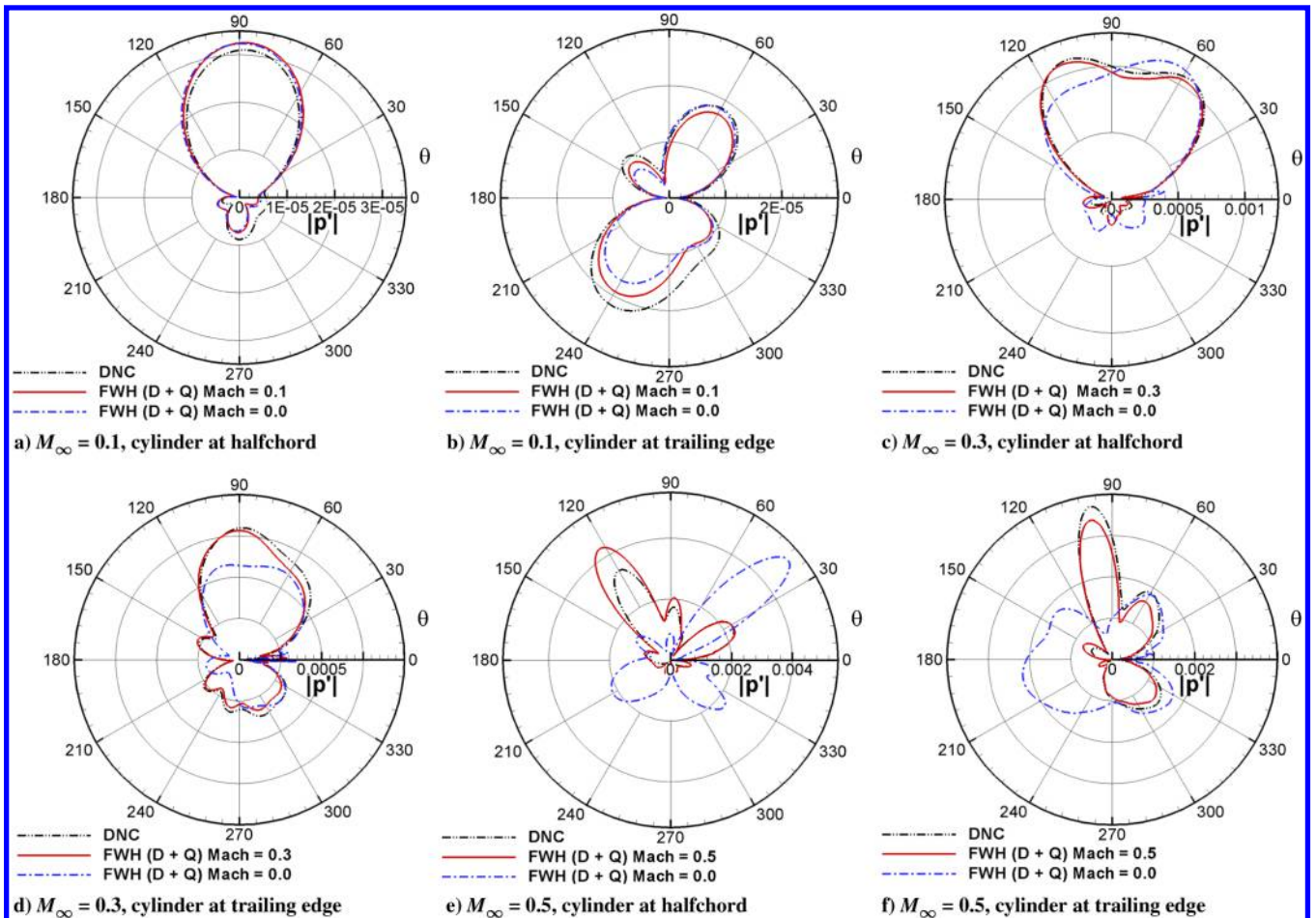


Fig. 18 Mean flow convection effects on FW-H acoustic prediction; results presented for the cylinder vortex shedding frequency.

predictions performed at observer positions $r/c = 2$ are sufficiently far from the source region. One should also mention that, at $M_\infty = 0.3$ and 0.5 , the present dipole and quadrupole sources are not compact for the cylinder vortex shedding frequency. Therefore, the typical compact dipole and quadrupole power law scalings for acoustic intensity should not be observed. Finally, in Fig. 18, one can observe the effects of including mean flow convection in the acoustic propagation for different freestream Mach numbers. The acoustic predictions in this figure are obtained for the cylinder vortex shedding frequency for cases 1 to 6. In this figure, results are also presented for the case in which no mean flow contributions are included in the acoustic propagation formulation. This means that M is set to zero in the convective Green's function, Eq. (5), applied in the present implementation of the FW-H equation. Such results are referred to in the figure as the zero Mach number case. For low Mach numbers, mean flow convection has negligible impact on the total noise radiation. However, for $M_\infty = 0.3$ and 0.5 , the lack of convection effects modify the acoustic pressure directivities and, in order to have accurate predictions, these effects should be included in the FW-H equation.

D. Quadrupole Sources

Figure 19 presents acoustic pressure directivities, in log-scale, obtained for the separate terms appearing in the quadrupole sources, namely Reynolds stresses ($\rho u_i u_j$), entropy fluctuations ($p' - c_0^2 \rho'$) and viscous stresses (τ_{ij}). This figure allows one to estimate the individual noise contributions from each of these terms and, therefore, to assess their importance in the quadrupole calculations. In Figs. 19a and 19b, one can see directivity plots computed for the airfoil and cylinder vortex shedding frequencies, respectively, for

$M_\infty = 0.3$, and, in Figs. 19c and 19d, similar results for $M_\infty = 0.5$ are presented. For all solutions shown in Fig. 19, the cylinder is positioned at the airfoil trailing edge. For all figures in this subsection, observers are located at $r/c = 2$. From these figures, it is possible to observe that the Reynolds stresses are the dominant terms in the noise radiated by quadrupole sources, in accordance with results in Lighthill's work [1]. Despite the low Reynolds number flows, one can see that viscous stresses have negligible contribution to far-field noise. Likewise, entropy fluctuations add a negligible contribution to far-field noise, except at the downstream direction.

A comparison of pressure amplitudes between Figs. 19a and 19b, and Figs. 19c and 19d, show that, for a fixed freestream Mach number, quadrupole sources radiate higher noise levels at higher frequencies. As expected, a similar comparison in terms of freestream Mach numbers between Figs. 19a and 19c, and Figs. 19b and 19d, show that higher noise levels are radiated for higher speed flows.

In Figs. 20 and 21, field plots of Reynolds stresses are shown for the airfoil and cylinder vortex shedding frequencies, respectively. In these figures, the cylinder is at the trailing-edge position. In order to compare the spatial distribution of the separate Reynolds stress terms, $|\rho u_i u_j|$, for different Mach numbers, these noise sources are normalized by freestream values for each flow configuration. These figures allow an assessment of Mach number effects on the spatial distribution of quadrupole sources due to Reynolds stresses.

Figure 20 shows that, for the airfoil vortex shedding frequency, the normalized source distributions for Mach numbers 0.1 and 0.3 are similar along the airfoil and cylinder wake regions for all Reynolds stress terms. However, for Mach 0.5, higher peak values of $|\rho u_1 u_1|$ and $|\rho u_1 u_2|$ are observed along the cylinder wake region. It is interesting to notice that, although the Reynolds stresses are computed at the airfoil vortex shedding frequency, in Fig. 20, it is possible

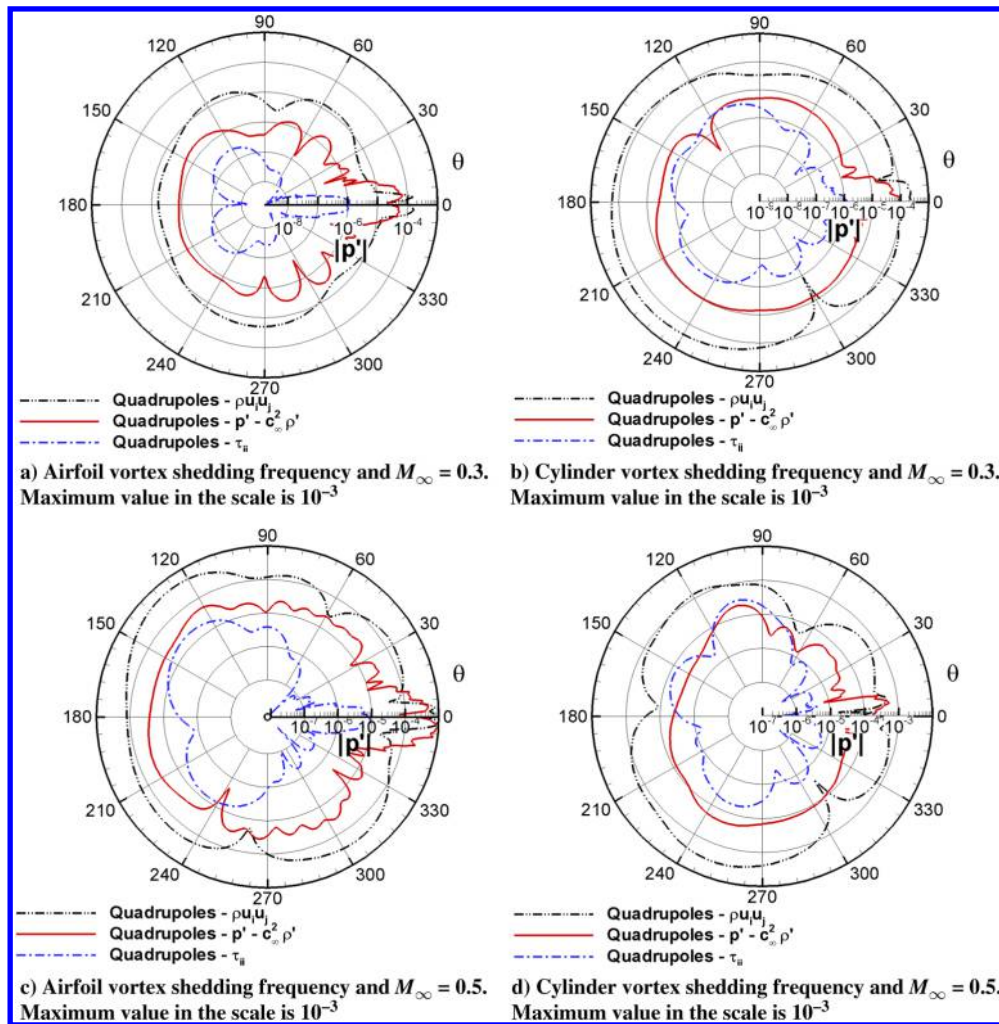


Fig. 19 Directivity plots (in log-scale) of separate terms composing quadrupole sources for cylinder at trailing-edge position.

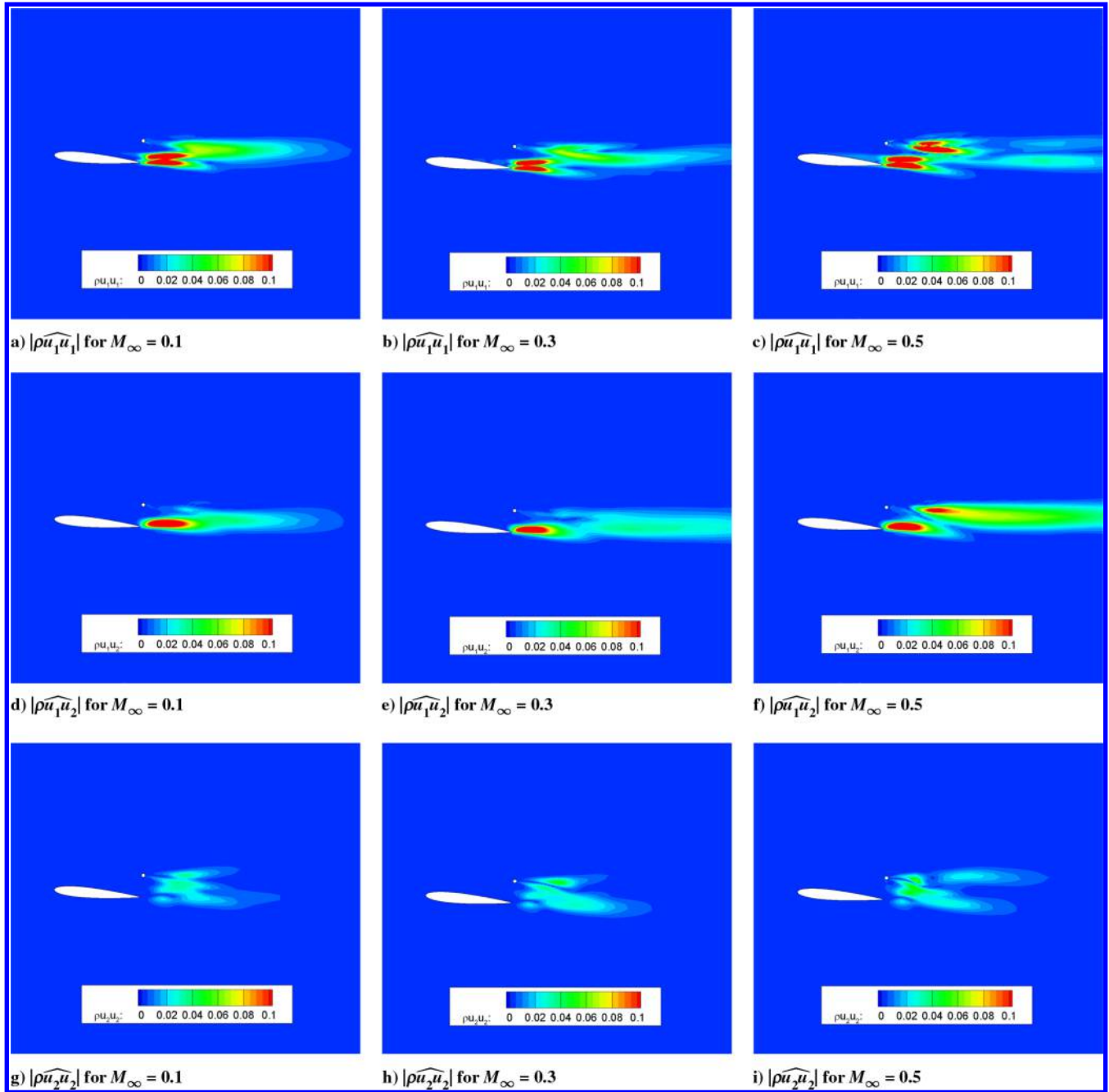


Fig. 20 Frequency domain Reynolds stresses normalized by freestream quantities for airfoil vortex shedding frequency and cylinder at trailing-edge position.

to see large values of Reynolds stress terms along the cylinder wake region. For $M_\infty = 0.5$, these values are comparable to those calculated along the airfoil wake region and a possible explanation for this effect would be wake interaction.

One can see in Fig. 21 that, for the cylinder vortex shedding frequency, magnitudes of Reynolds stresses are lower along the airfoil wake region. In the same figure, for all Mach numbers, similar values of $|\rho \widehat{u}_1 u_1|$ and $|\rho \widehat{u}_1 u_2|$ are observed along the cylinder wake region. Although similar levels of normalized Reynolds stresses are observed, the wake patterns show differences in length and it is possible to see a more pronounced wake truncation effect for $|\rho \widehat{u}_1 u_2|$ at $M_\infty = 0.5$.

V. Investigation of Noise-Source Mechanisms

The results presented in the previous sections showed a significant dependence of the sound radiation with respect to the freestream Mach number. In order to understand in more detail the role of

compressibility, the $M_\infty = 0.3$ and $M_\infty = 0.5$ flows are investigated here, with the cylinder at the trailing-edge position. For the first case, quadrupole radiation is relatively small, whereas for the higher Mach number flow, there is a substantial increase of the contribution of quadrupoles to the radiated sound.

A. Wave-Packet Structure of the Cylinder Wake

In Fig. 22, one can see the amplitude of pressure fluctuations for the cylinder vortex shedding frequency in the cylinder wake. The amplitude modulation of the fluctuations in the wake, shown in Fig. 22, and the visualizations of a wavy structure for the pressure fluctuations in Figs. 14a and 16a show that fluctuations in the wake can be described as a hydrodynamic wave-packet. In Fig. 22, it is possible to observe that, for $M_\infty = 0.3$, the wave-packet amplitudes are low and there is little amplitude growth far from the cylinder. For $M_\infty = 0.5$, substantially higher amplitudes are seen as well as a significant amplitude growth between $x/c = 0.6$ and $x/c = 0.8$. Another difference is related to the decay of the wave-packet. For the

$M_\infty = 0.5$ case, there is a sudden decay around $x/c = 0.85$. For the lower Mach number, the decay is smooth, and the wave-packet extends downstream of $x/c = 1$. In order to further investigate the changes in cylinder wake structure, simulations of the flow past an isolated cylinder are performed. With such results, one can eliminate any effects of wake interaction potentially present in previously analyzed cases. Figures 23 and 24 show results of acoustic predictions for $M_\infty = 0.3$ and 0.5, respectively, for the vortex shedding frequency. As presented in Figs. 23a and 24a, the typical dipole radiation pattern can be observed, similarly to Inoue and Hatakeyama [24]. The individual contributions of the surface dipole and volume quadrupole sources are presented in Figs. 23b and 24b. In these plots, directivities are computed for observers at $10d$ away from the cylinder center. Although quadrupole effects become more prominent for higher Mach numbers, dipole sources are still dominant. Furthermore, for a single cylinder, compact dipole and quadrupole patterns are observed even for moderate Mach numbers. Comparison of acoustic predictions obtained by direct noise calculation and the FW–H acous-

tic analogy are presented in Figs. 23c and 24c and good agreement is achieved when all sources are included in the computation. From the above observations, one can conclude that quadrupole radiation increases with Mach number as expected from aeroacoustics theory [21]. However, for a single cylinder, this increase has a smaller effect on total far-field prediction than that for a configuration composed of cylinder plus airfoil (see for instance Figs. 16 and 24).

Figure 25 shows a comparison of amplitude of pressure fluctuations along the wake of a single cylinder for the vortex shedding frequency. In Figs. 25a and 25b, results are presented for $M_\infty = 0.3$ and $M_\infty = 0.5$, respectively. In order to compare the current results with those from Fig. 22, the x coordinate is scaled by chord length and pressure fluctuations are scaled by freestream dynamic pressure. For both Mach numbers tested, it is possible to see that, near the cylinder, the spatial distribution of amplitude of pressure fluctuations are similar to those for the case with wake interaction. However, further downstream, wake patterns for a single cylinder show a slow amplitude decay. These results reinforce the previous

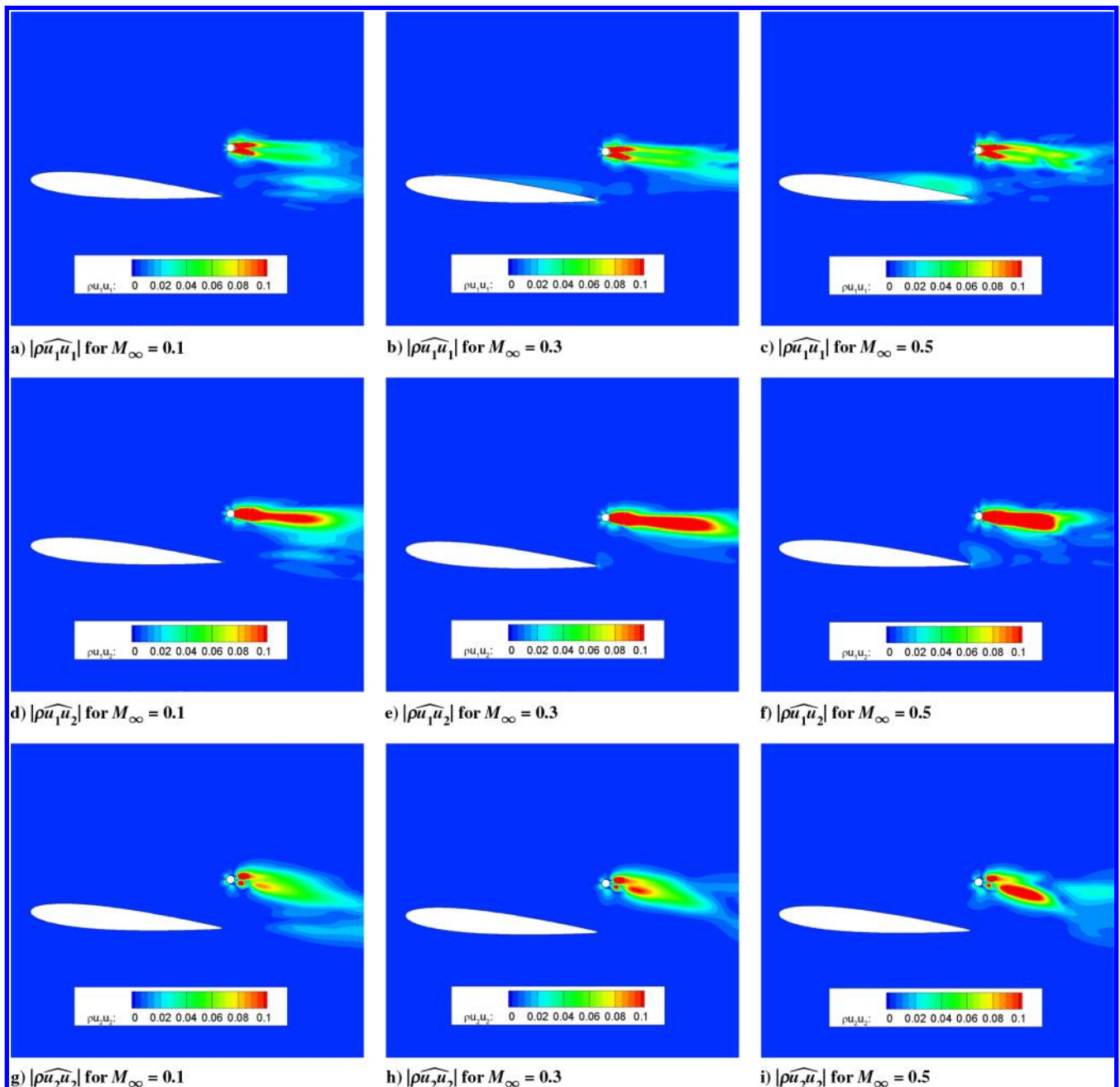


Fig. 21 Frequency domain Reynolds stresses normalized by freestream quantities for cylinder vortex shedding frequency and cylinder at trailing-edge position.

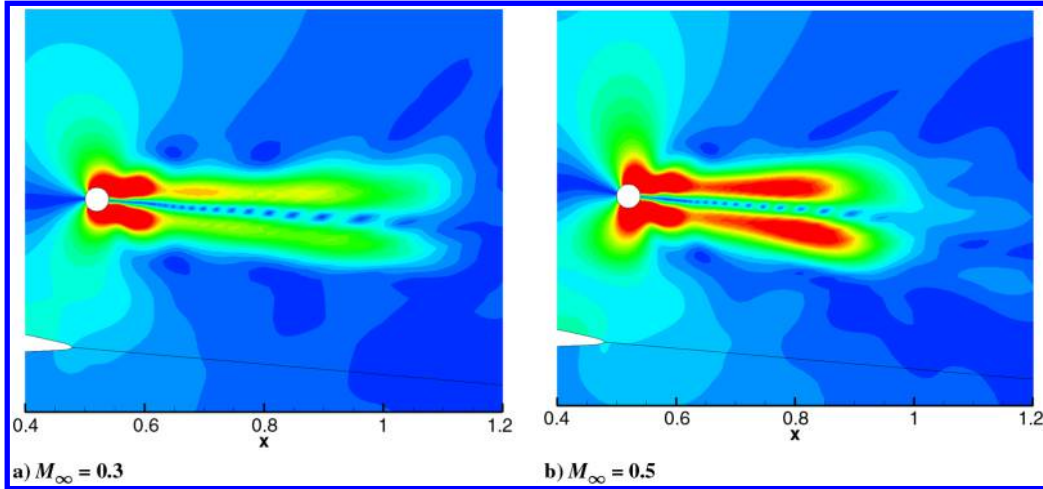


Fig. 22 Amplitude of pressure fluctuations for the cylinder vortex shedding frequency.

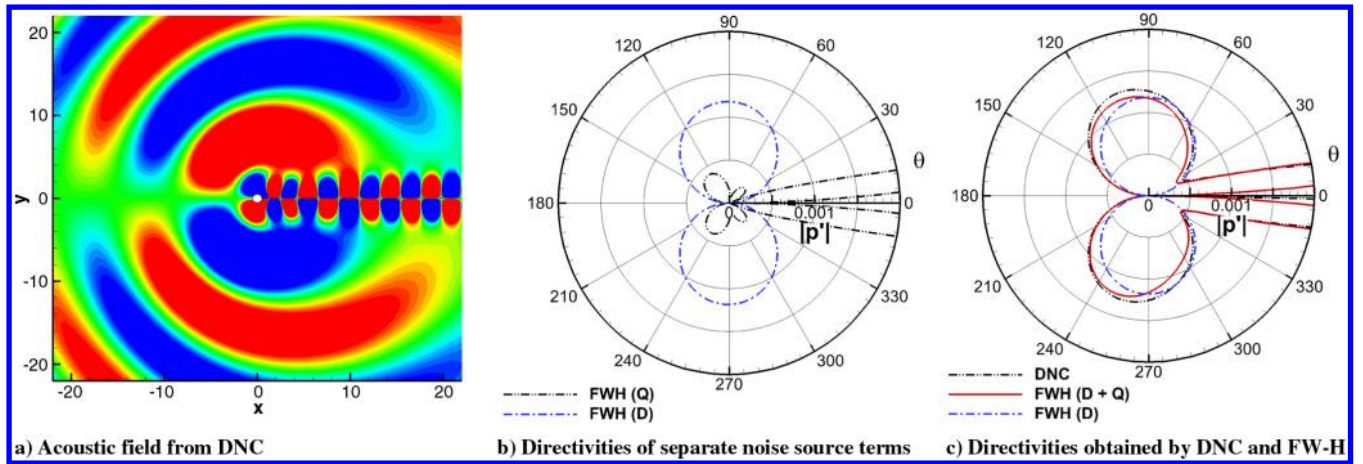


Fig. 23 Acoustic predictions for isolated cylinder at $M_\infty = 0.3$ and vortex shedding frequency.

comments regarding the truncation of pressure fluctuations along the wake region for the cases with wake interaction. In the following section, the linear stability of the cylinder wakes is studied for the cylinder — airfoil case. This analysis will improve the understanding of the differences between the two flows analyzed at $M_\infty = 0.3$ and 0.5.

B. Linear Stability Analysis of the Cylinder Wake

1. Mathematical Model

Considering linearized inviscid disturbances in a parallel, sheared flow with velocity profile $U(y)$, and that the pressure fluctuations are given as

$$p'(x, y, t) = p(y) \exp[i(\alpha x - \omega t)] \tag{6}$$

the Rayleigh equation is obtained, which for compressible flow is given as [25]

$$\frac{d^2 p}{dy^2} - \frac{2U}{U-c} \frac{dp}{dy} - \alpha^2 [1 - M^2(U-c)^2] p = 0 \tag{7}$$

where the mean flow is assumed as isothermal since the maximum mean temperature difference computed along the cylinder wake region is 0.3%. In the previous equation, $c = \omega/\alpha$ is the complex-valued phase speed of the instability wave. When spatially growing

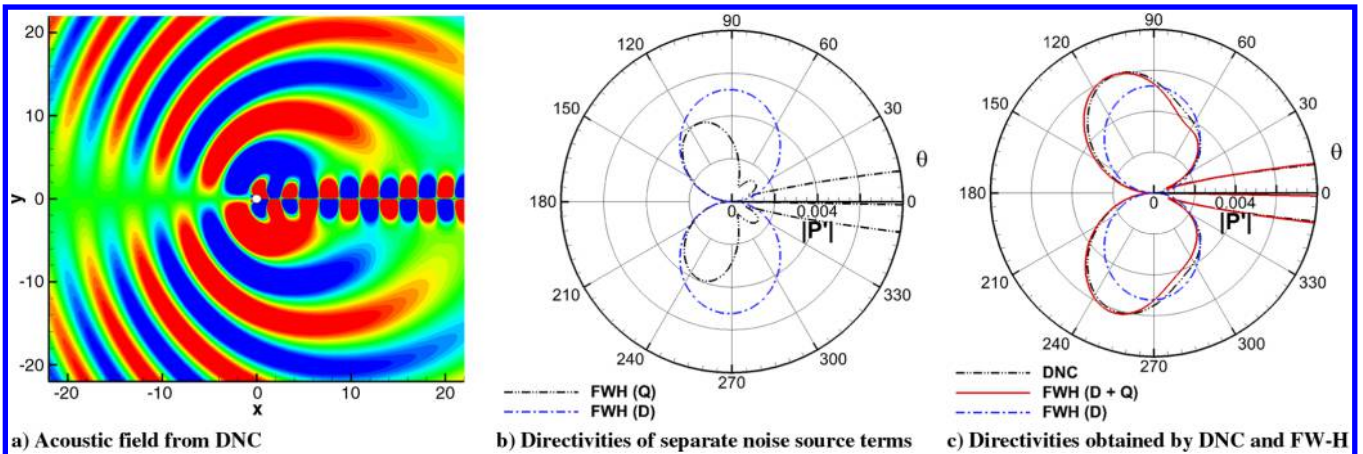


Fig. 24 Acoustic predictions for isolated cylinder at $M_\infty = 0.5$ and vortex shedding frequency.

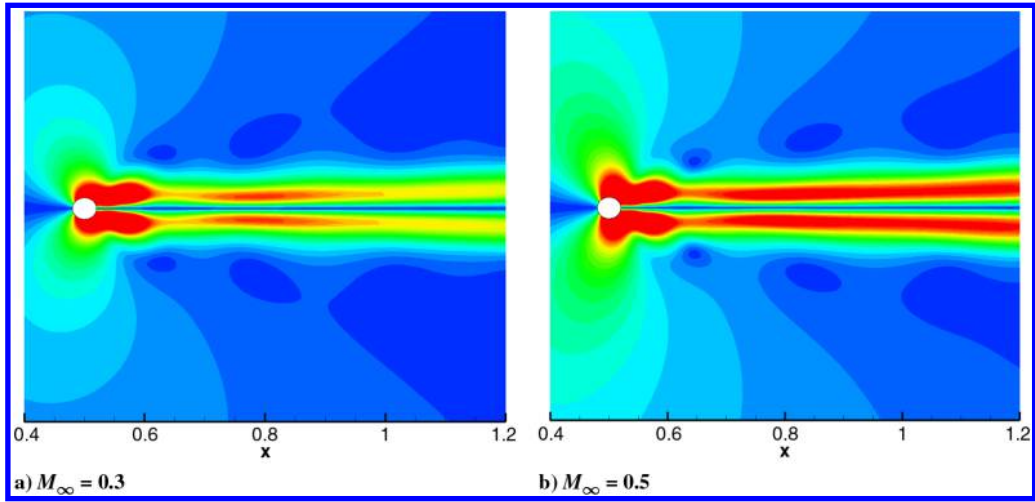


Fig. 25 Amplitude of pressure fluctuations for the cylinder vortex shedding frequency (single cylinder case).

or decaying disturbances are considered, the frequency ω is a given real quantity and the wavenumber $\alpha = \alpha_r + i\alpha_i$ is a complex-valued eigenvalue. The negative of its imaginary part, $-\alpha_i$, is the spatial growth rate of the instability wave.

This analysis, based on spatial growth or decay of upstream disturbances, is appropriate for convectively unstable flows. However, it is well known that a parallel-flow analysis of the stability of the cylinder wake may reveal an absolute instability, where the linear impulse response of the base flow comprises temporal growth at a fixed position and a feedback from downstream disturbances becomes possible (see Huerre and Monkewitz [26] for a review). In this case, the results of a spatial stability analysis considering real-valued frequencies are questionable, as the feedback mechanism within the flow, which cannot be modeled using spatial stability, is essential in the determination of the evolution of disturbances. When such a parallel-flow analysis is performed for the cylinder wake, it is found that stations close to the cylinder are absolutely unstable, and velocity profiles for downstream stations are convectively unstable. This leads to the picture that self-excited oscillations appear near the cylinder due to the absolute instability and, for downstream stations, the fluctuations generated near the cylinder are amplified and convected downstream [27].

In the present work, the authors are not concerned with the generation of the vortex street, which is usually associated with absolute instabilities [28]. Rather, they are concerned with the spatial evolution of the fluctuations in the wake for downstream stations such as the spatial amplification, saturation and decay of disturbances. Hence, the current focus is on downstream positions of the wake, where only convective instability is expected. In this case, an analysis based on spatial stability is appropriate. All the results in this section are obtained for $x/c = 0.7$ or greater, which means that the spatial stability problem is solved for positions at least 5 diameters downstream of the cylinder, which was previously shown as a region of convective instability [27]. Moreover, velocity profiles from the simulation are characterized by calculating the parameter

$$\Lambda = \frac{U_c - U_{\max}}{U_c + U_{\max}} \quad (8)$$

analyzed by Monkewitz [28], where U_c is the velocity at the center of the wake and U_{\max} is the freestream velocity. For the stations studied in this work, the minimal value of Λ is found to be -0.81 , and absolute instability in several velocity profiles of wakes is only found for Λ lower than about -0.85 for any Reynolds number [28]. Based on these observations, one can consider that the spatial stability analysis is appropriate to study the fluctuations in the downstream cylinder wake.

2. Numerical Methods

The eigenvalue problem in Eq. (7) is solved directly using a pseudo-spectral method to discretize the derivatives [29]. Calculations are performed with 200 Chebyshev polynomials and the infinite domain is mapped into $[-1, 1]$ by the change of variables

$$z = \frac{Ly}{\sqrt{1-y^2}} \quad (9)$$

as suggested by Boyd [30]. Here, $L = 0.5$ is chosen to provide accurate resolution of the wake profiles for test cases 5 and 6 of Table 1. The velocity profile, $U(y)$, downstream of the airfoil and the cylinder is given by an interaction of both cylinder and airfoil wakes. This velocity profile is fitted using the function

$$U(y) = 1 - Q_1 \operatorname{sech}((y - y_{c1})/L_1)^2 - Q_2 \operatorname{sech}((y - y_{c2})/L_2)^2 \quad (10)$$

This fit is performed for the values of x/c specified in the next section. The parameters Q_1 , Q_2 , y_{c1} , y_{c2} , L_1 and L_2 of Eq. (10) are obtained by a nonlinear least-squares fit of the velocity profiles from the numerical calculation, referred to as DNS in the figures. Two sample fits are shown in Fig. 26, where we see that the velocity profile is accurately represented by the expression in Eq. (10).

The eigenvalue problem in Eq. (7) is nonlinear in α . To solve it using standard linear eigenvalue routines, the following transformation is applied

$$\begin{bmatrix} 0 & \mathcal{I} & 0 \\ 0 & 0 & \mathcal{I} \\ -\mathcal{F}_0 & -\mathcal{F}_1 & -\mathcal{F}_2 \end{bmatrix} \begin{bmatrix} p \\ \alpha p \\ \alpha^2 p \end{bmatrix} = \alpha \begin{bmatrix} \mathcal{I} & 0 & 0 \\ 0 & \mathcal{I} & 0 \\ 0 & 0 & \mathcal{F}_3 \end{bmatrix} \begin{bmatrix} p \\ \alpha p \\ \alpha^2 p \end{bmatrix} \quad (11)$$

where \mathcal{I} is the identity operator and \mathcal{F}_i are operators for terms of the equation with order i in α . The \mathcal{F}_i operators are given as

$$\mathcal{F}_3 = -U\mathcal{I} + U^3 M^2 \mathcal{I} \quad (12)$$

$$\mathcal{F}_2 = \omega \mathcal{I} - 3U^2 \omega M^2 \mathcal{I} \quad (13)$$

$$\mathcal{F}_1 = U \frac{d^2}{dy^2} - 2U' \frac{d}{dy} + 3U\omega^2 M^2 \mathcal{I} \quad (14)$$

$$\mathcal{F}_0 = -\omega \frac{d^2}{dy^2} - \omega^2 M^2 \mathcal{I} \quad (15)$$

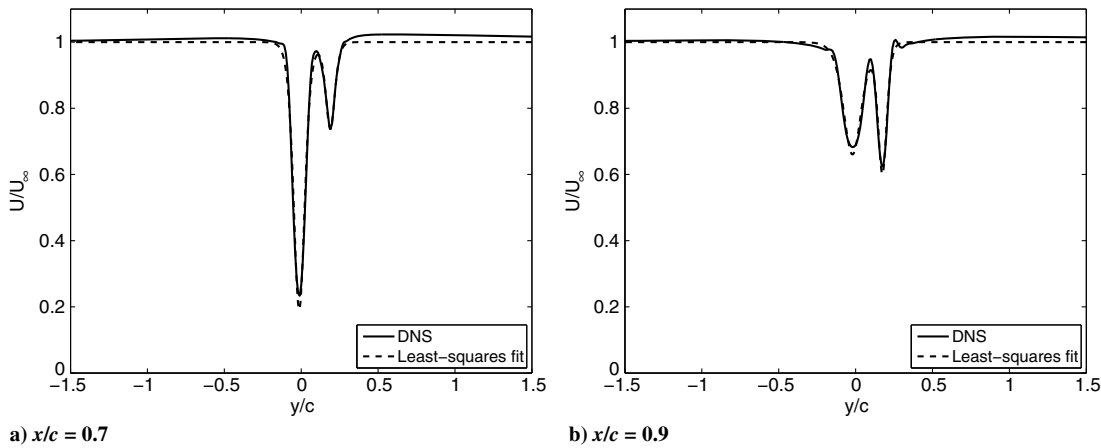


Fig. 26 Comparison of velocity profiles obtained by flow simulation (DNS) and least-squares fit.

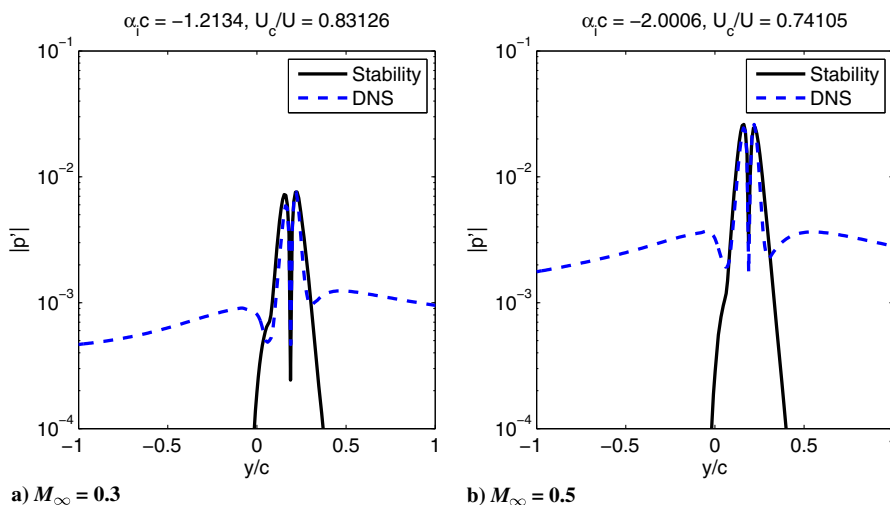


Fig. 27 Comparison between numerical calculations (DNS) and linear stability results at $x/c = 0.7$.

A similar approach was used and validated in previous work which dealt with the linear stability of shear layers [31].

3. Linear Stability Results

The most unstable eigenfunction obtained in the stability analysis is compared with the pressure fluctuations in the numerical flow simulation. For all cases analyzed, the eigenspectrum presented only one unstable mode. Throughout this section, the analysis is per-

formed for the fluctuations at the cylinder vortex shedding frequency. This is the most favorable case for the linear stability analysis assuming parallel flow, since the higher frequency is associated with a smaller wavelength and changes of the mean flow in the wavelength scale become negligible. Figure 27 shows this comparison at $x/c = 0.7$. The double bump observed in the numerical simulation results is accurately reproduced by the linear stability eigenfunction for both Mach numbers. For high $|y/c|$, the pressure fluctuations in

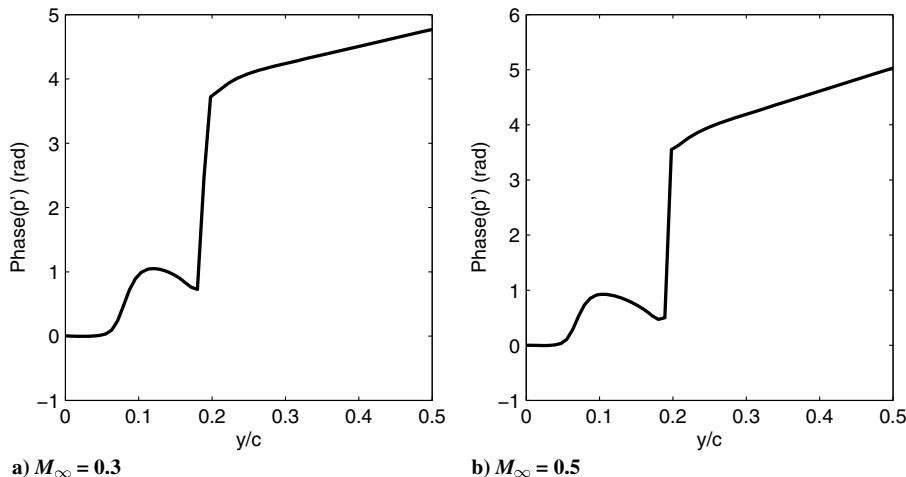


Fig. 28 Phases of the linear stability eigenfunction at $x/c = 0.7$.

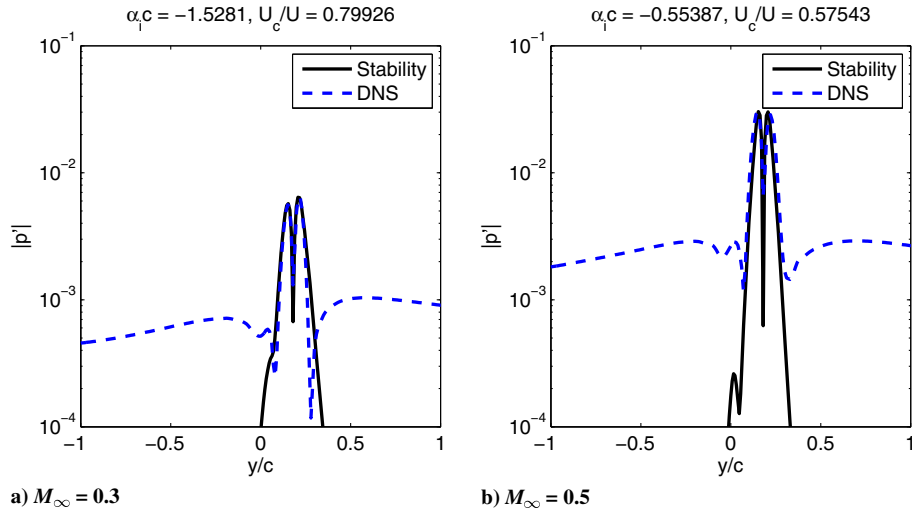


Fig. 29 Comparison between numerical calculations (DNS) and linear stability results at $x/c = 0.8$.

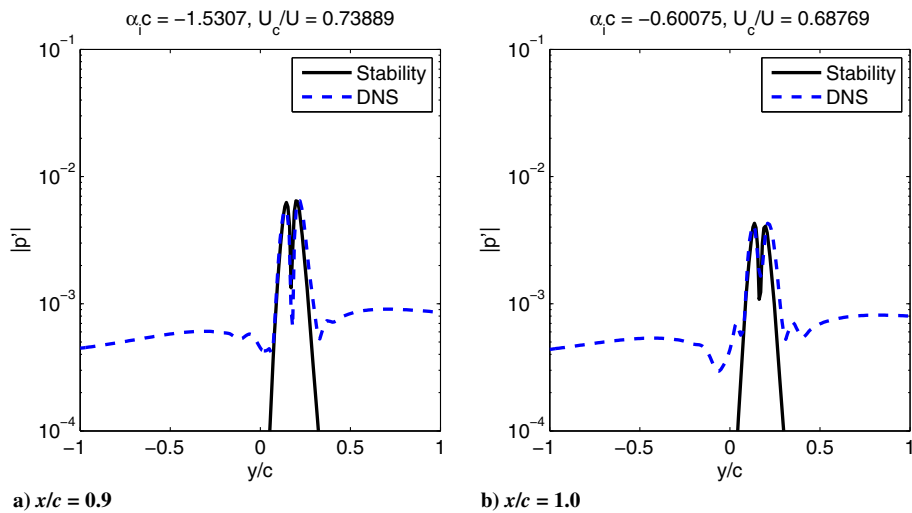


Fig. 30 Comparison between numerical calculations (DNS) and linear stability results for $M_\infty = 0.3$. Similar analysis performed for $M_\infty = 0.5$ revealed only stable modes.

the computational results, referred to as DNS in the figures, are acoustic waves which cannot be obtained using parallel-flow stability calculations.

The cited double bump can be related to the von Kármán vortex street behind the cylinder. Figure 28 shows the phases of the stability eigenfunction. For both Mach numbers, there is a phase jump of approximately π around $y/c = 0.2$, which corresponds to the center of the wake. This phase opposition between the two sides of the wake is expected for the antisymmetric von Kármán vortex street. There is a significant compressibility effect in the growth rates for the two cases, which are given by $\alpha_1 c = -1.2134$ for $M_\infty = 0.3$ and $\alpha_1 c = -2.0006$ for $M_\infty = 0.5$. Such growth rates can be related to the maximum amplitudes of the wave-packets in the cylinder wake. One should recall that, for $M_\infty = 0.5$, higher amplifications are seen in Fig. 22.

Figure 29 shows a similar comparison, this time performed for $x/c = 0.8$. As in the previous position, the linear stability eigenfunction represents accurately the pressure fluctuations in the cylinder wake. However, this time, the growth rate for $M_\infty = 0.5$ is lower than that for $M_\infty = 0.3$. These results can be observed in Fig. 29. As one moves downstream, the $M_\infty = 0.3$ wake continues to present an unstable mode. This behavior is confirmed by the stability analysis at $x/c = 0.9$ and $x/c = 1.0$, shown in Fig. 30. On the other hand, for the $M_\infty = 0.5$ flow, there are only stable modes which lead to a spatial decay of the wave-packet in this region. This explains the

sudden truncation of the $M_\infty = 0.5$ wave-packet and the downstream persistence of the wave-packet for $M_\infty = 0.3$.

The agreement between the calculated eigenfunctions and the pressure fluctuations in the numerical calculations shows that linear stability is an appropriate framework to study the fluctuations in the cylinder wake. Based on these results, one can cite the following reasons which explain the higher sound emission by the wake of the $M_\infty = 0.5$ test case. Initially, near the cylinder, the $M_\infty = 0.5$ wave presents higher spatial amplification, which leads to higher fluctuation amplitudes if compared to the $M = 0.3$ case. As one moves downstream, the $M_\infty = 0.5$ wave-packet undergoes a sudden truncation, which is known to result in an increased sound radiation [32]. Finally, for $M_\infty = 0.5$, the convective Mach numbers, which can be obtained as $M_c = (U_c/U)M_\infty$, are higher than in the $M_\infty = 0.3$ case.

VI. Conclusions

The current work presents aeroacoustic predictions of a model airframe noise problem in order to assess the effects of wake interaction on both the flow and acoustic fields. Simulations of unsteady flows are performed for a two-dimensional configuration composed of a cylinder placed above a NACA 0012 airfoil at 5 deg angle of incidence and for a single cylinder. Although simulations are two-dimensional, similar aerodynamic and aeroacoustic physical mechanisms are found in three-dimensional computations of similar

configurations [12,13] and the present analysis is relevant in the context of vortex shedding tonal noise generation. Numerical calculations include both noise generation and its subsequent propagation to the far field. For all test cases, the Reynolds number based on the airfoil chord is set at $Re_c = 5000$ and the Reynolds number based on the diameter of the cylinder is $Re_d = 200$. An assessment of cylinder position and freestream Mach number effects on sound radiation is performed for $M_\infty = 0.1, 0.3, \text{ and } 0.5$. The investigation of the noise sources for airfoil and cylinder vortex shedding frequencies is presented using a hybrid methodology which employs direct calculation for near field source computations and the FW–H equation as the acoustic analogy formulation. In order to verify the numerical solutions, acoustic prediction results obtained by DNC are compared to those computed by the FW–H equation and good agreement is observed.

The results indicate that, when the cylinder vortex shedding is the driving noise source mechanism, intense dipolar interference occurs for all configurations analyzed. When the cylinder is positioned at half-chord location, acoustic scattering along the airfoil surface is more pronounced and dipolar interference is constructive above the airfoil, increasing noise radiation upwards. Underneath the airfoil, dipole sources are out of phase and noise radiation is reduced in that direction. When the cylinder is located above the trailing edge, dipolar interference presents more complicated patterns with combined diffraction and reflection effects.

The separate contributions of the terms composing the quadrupole sources are analyzed. Even for the low Reynolds number flows investigated, Reynolds stresses are the dominant quadrupole noise sources and viscous effects as well as entropy fluctuations can be neglected. A comparison of pressure amplitudes show that, for a fixed freestream Mach number, quadrupole sources radiate higher noise levels at higher frequencies. A similar comparison in terms of freestream Mach numbers shows that higher quadrupole noise levels are radiated for higher speed flows. The results in terms of spatial distribution of Reynolds stresses, which are the most relevant terms in quadrupole sources, also indicate that there are significant wake interaction effects for the higher Mach number here considered. It is demonstrated that, for the airfoil VS frequency, there is significant increase in the amplitude of the quadrupole sources at the cylinder wake at higher Mach numbers. It is found that while quadrupole sources can be neglected in noise predictions by the FW–H equation for the $M_\infty = 0.1$ flow calculations, they should be included for the $M_\infty = 0.3$ and 0.5 acoustic predictions at low and high frequencies. For low Mach numbers, mean flow convection has negligible impact on the total noise radiation. However, for $M_\infty = 0.3$ and 0.5 , convection effects considerably modify the acoustic pressure directivities and accurate predictions require the inclusion of these effects in the FW–H equation.

For moderate Mach number flows with wake interaction, quadrupole sources become important to the total acoustic prediction, specially for the downward noise radiation. For the single cylinder case, quadrupole radiation is less pronounced than that for the case with wake interaction. It is also observed that, for the cylinder plus airfoil case, there is a sudden truncation of the cylinder wake for the cylinder VS frequency. This truncation effect is not observed for the isolated cylinder. This difference between the flows suggests that the observed wake truncation in the cylinder-airfoil problem leads to the increase in quadrupole radiation.

This issue is further investigated using a linear stability analysis for the wake interaction problem. This is seen to be adequate for the present flow due to the close agreement between the stability eigenfunctions and the fluctuations in the cylinder wake. It is seen that, for the higher Mach number, compressibility effects lead to the formation of a wave-packet with higher maximum amplitude, higher convection Mach number and a sudden spatial decay, all of which should lead to an increase of quadrupole radiation.

In summary, this model airframe noise problem consisting of the interaction of two wakes shows major differences in noise radiation when compared to the case of an isolated cylinder at similar flow conditions. It is observed that wake interaction becomes a major feature of the flow, causing a faster downstream decay of convecting

disturbances. Compressibility effects also play a role and contribute to this decay as observed in DNS and stability analysis. This decay, observed in the form of wake truncation, is proposed as responsible for the significant increase of quadrupole noise radiation.

Acknowledgments

The authors acknowledge the financial support received from Fundação de Amparo à Pesquisa do Estado de São Paulo, FAPESP, under Grants No. 2013/03413-4 and No. 2013/07375-0, and the financial support received from Conselho Nacional de Desenvolvimento Científico e Tecnológico, CNPq, under Grants No. 470695/2013-7 and No. 309985/2013-7. The authors also acknowledge the FAEPEX M.Sc., fellowship provided to Bruno Backes by Pró-Reitoria de Pesquisa of University of Campinas, PRP-UNICAMP. The computational resources provided by CENAPAD-SP under Project No. 551 are also acknowledged.

References

- [1] Lighthill, M. J., "On Sound Generated Aerodynamically. I. General Theory," *Proceedings of the Royal Society of London. Series A: Mathematical and Physical Sciences*, Vol. 211, No. 1107, 1952, pp. 564–587. doi:10.1098/rspa.1952.0060.
- [2] Ffowcs Williams, J. E., and Hawkings, D. L., "Sound Generation by Turbulence and Surfaces in Arbitrary Motion," *Royal Society of London Philosophical Transactions Series A*, Vol. 264, No. 1151, 1969, pp. 321–342. doi:10.1098/rsta.1969.0031
- [3] Wolf, W. R., Azevedo, J. L. F., and Lele, S. K., "Convective Effects and the Role of Quadrupole Sources for Aerofoil Aeroacoustics," *Journal of Fluid Mechanics*, Vol. 708, Oct. 2012, pp. 502–538. doi:10.1017/jfm.2012.327
- [4] Wolf, W. R., Azevedo, J. L. F., and Lele, S. K., "Effects of Mean Flow Convection, Quadrupole Sources and Vortex Shedding on Airfoil Overall Sound Pressure Level," *Journal of Sound and Vibration*, Vol. 332, No. 26, Dec. 2013, pp. 6905–6912. doi:10.1016/j.jsv.2013.08.029
- [5] Wolf, W. R., and Lele, S. K., "Acoustic Analogy Formulations Accelerated by Fast Multipole Method for Two-Dimensional Aeroacoustic Problems," *AIAA Journal*, Vol. 48, No. 10, 2010, pp. 2274–2285. doi:10.2514/1.J050338
- [6] Wolf, W. R., and Lele, S. K., "Aeroacoustic Integrals Accelerated by Fast Multipole Method," *AIAA Journal*, Vol. 49, No. 7, 2011, pp. 1466–1477. doi:10.2514/1.J050861
- [7] Casper, J. H., Lockard, D. P., Khorrami, M. R., and Streett, C. L., "Investigation of Volumetric Sources in Airframe Noise Simulations," *10th AIAA/CEAS Aeroacoustics Conference and Exhibit*, AIAA, Reston, VA, 2004.
- [8] Greschner, B., Thiele, F., Jacob, M. C., and Casalino, D., "Prediction of Sound Generated by a Rod-Airfoil Configuration Using EASM DES and the Generalised Lighthill/FW–H Analogy," *Computers & Fluids*, Vol. 37, No. 4, 2008, pp. 402–413. doi:10.1016/j.compfluid.2007.02.013
- [9] Spalart, P. R., "On the Precise Implications of Acoustic Analogies for Aerodynamic Noise at Low Mach Numbers," *Journal of Sound and Vibration*, Vol. 332, No. 11, 2013, pp. 2808–2815. doi:10.1016/j.jsv.2012.12.029
- [10] Jacob, M. C., Boudet, J., Casalino, D., and Michard, M., "A Rod-Airfoil Experiment as Benchmark for Broadband Noise Modeling," *Theoretical and Computational Fluid Dynamics*, Vol. 19, No. 11, 2005, pp. 171–196. doi:10.1007/s00162-004-0108-6
- [11] Yu, C., Wolf, W. R., and Lele, S. K., "Quadrupole Noise in Turbulent Wake Interaction Problems," *18th AIAA/CEAS Aeroacoustics Conference and Exhibit*, AIAA, Reston, VA, June 2012.
- [12] Yu, C., and Lele, S. K., "Volume Noise Sources in Turbulent Wake Interaction Problems: True Quadrupole Noise?" *20th AIAA/CEAS Aeroacoustics Conference and Exhibit*, AIAA, Reston, VA, June 2014.
- [13] Yu, C., "Turbulent Wake Interaction LES and Aeroacoustic Predictions," Ph.D. Thesis, Stanford Univ., Stanford, CA, 2014.
- [14] Nagarajan, S., Lele, S. K., and Ferziger, J. H., "A Robust High-Order Compact Method for Large Eddy Simulation," *Journal of Computa-*

- tional Physics*, Vol. 191, No. 2, 2003, pp. 392–419.
doi:10.1016/S0021-9991(03)00322-X
- [15] Bhaskaran, R., and Lele, S. K., “Large Eddy Simulation of Free-Stream Turbulence Effects on Heat Transfer to a High-Pressure Turbine Cascade,” *Journal of Turbulence*, Vol. 11, No. 6, 2010, pp. 1–15.
doi:10.1080/14685241003705756
- [16] Lele, S. K., “Compact Finite Difference Schemes with Spectral-Like Resolution,” *Journal of Computational Physics*, Vol. 103, No. 1, 1992, pp. 16–42.
doi:10.1016/0021-9991(92)90324-R
- [17] Beam, R. M., and Warming, R. F., “An Implicit Factored Scheme for the Compressible Navier–Stokes Equations,” *AIAA Journal*, Vol. 16, No. 4, 1978, pp. 393–402.
doi:10.2514/3.60901
- [18] Lockard, D. P., “An Efficient, Two-Dimensional Implementation of the Ffowcs Williams and Hawkins Equation,” *Journal of Sound and Vibration*, Vol. 229, No. 4, 2000, pp. 897–911.
doi:10.1006/jsvi.1999.2522
- [19] Driver, D. M., and Mateer, G. G., “Wake Flow in Adverse Pressure Gradient,” *Heat and Fluid Flow*, Vol. 23, No. 5, 2002, pp. 564–571.
doi:10.1016/S0142-727X(02)00152-2
- [20] Tummers, M. J., Passchier, D. M., and Bakker, P. G., “Experiments on the Turbulent Wake of a Flat Plate in a Strong Adverse Pressure Gradient,” *Heat and Fluid Flow*, Vol. 28, No. 1, 2007, pp. 145–160.
doi:10.1016/j.ijheatfluidflow.2006.02.028
- [21] Curle, N., “The Influence of Solid Boundaries Upon Aerodynamic Sound,” *Proceedings of the Royal Society of London. Series A: Mathematical and Physical Sciences*, Vol. 231, No. 1187, 1955, pp. 505–514.
doi:10.1098/rspa.1955.0191
- [22] Ffowcs Williams, J. E., and Hall, L. H., “Aerodynamic Sound Generation by Turbulent Flow in the Vicinity of a Scattering Half Plane,” *Journal of Fluid Mechanics*, Vol. 40, No. 4, 1970, pp. 657–670.
doi:10.1017/S0022112070000368
- [23] Wolf, W. R., and Lele, S. K., “Fast Acoustic Scattering Simulations with Non-Uniform Flow Effects,” *16th AIAA/CEAS Aeroacoustics Conference and Exhibit*, AIAA, Reston, VA, 2010.
- [24] Inoue, O., and Hatakeyama, N., “Sound Generation by a Two-Dimensional Circular Cylinder in a Uniform Flow,” *Journal of Fluid Mechanics*, Vol. 471, Nov. 2002, pp. 285–314.
doi:10.1017/S0022112002002124
- [25] Criminale, W. O., Jackson, T. L., and Joslin, R. D., *Theory and Computation of Hydrodynamic Stability*, Cambridge Univ. Press, Cambridge, England, U.K., 2003.
- [26] Huerre, P., and Monkewitz, P. A., “Local and Global Instabilities in Spatially Developing Flows,” *Annual Review of Fluid Mechanics*, Vol. 22, No. 1, 1990, pp. 473–537.
doi:10.1146/annurev.fl.22.010190.002353
- [27] Triantafyllou, G. S., Triantafyllou, M. S., and Chryssostomidis, C., “On the Formation of Vortex Streets Behind Stationary Cylinders,” *Journal of Fluid Mechanics*, Vol. 170, No. 1, 1986, pp. 461–477.
doi:10.1017/S0022112086000976
- [28] Monkewitz, P. A., “The Absolute and Convective Nature of Instability in Two-Dimensional Wakes at Low Reynolds Numbers,” *Physics of Fluids*, Vol. 31, No. 5, 1988, pp. 999–1006.
doi:10.1063/1.866720
- [29] Trefethen, L. N., *Spectral Methods in MATLAB*, Vol. 10, Soc. for Industrial Mathematics, Philadelphia, 2000, pp. 51–56.
- [30] Boyd, J. P., *Chebyshev and Fourier Spectral Methods*, Dover Publ., Mineola, NY, 2001, p. 556.
- [31] Cavalieri, A. V. G., and Agarwal, A., “The Effect of Base-Flow Changes in Kelvin-Helmholtz Instability,” *19th AIAA/CEAS Aeroacoustics Conference and Exhibit*, AIAA, Reston, VA, May 2013.
- [32] Cavalieri, A. V. G., Jordan, P., Agarwal, A., and Gervais, Y., “Jittering Wave-Packet Models for Subsonic Jet Noise,” *Journal of Sound and Vibration*, Vol. 330, Nos. 18–19, 2011, pp. 4474–4492.
doi:10.1016/j.jsv.2011.04.007

D. Papamoschou
Associate Editor

This article has been cited by:

1. Antoine Hajczak, Laurent Sanders, François Vuillot, Philippe Druault. 2020. A comparison between off and on-body control surfaces for the FW-H equation: Application to a non-compact landing gear wheel. *Journal of Sound and Vibration* 115730. [[Crossref](#)]
2. Mauricio R. Massarotti, William Wolf. Passive and active methods to control the aeroacoustic noise generated by elliptical cylinders for automotive applications . [[Citation](#)] [[PDF](#)] [[PDF Plus](#)]
3. Maurício R. Massarotti, William R. Wolf. 2018. Aeroacoustic analysis of automotive roof crossbars through on-track acoustic measurements. *Applied Acoustics* 142, 95-105. [[Crossref](#)]